

JGR Earth Surface

RESEARCH ARTICLE

10.1029/2024JF007949

Key Points:

- A novel persistent homology-based method enables quantification of the spatiotemporal evolution of the slope deformation field
- The proposed method helps reveal critical precursory acceleration of deformation patterns long before the occurrence of landslides
- The spatiotemporal evolution of slope deformation underscores the long-range, effective predictions about its upcoming failure

Correspondence to:

G. Ma,
magang630@whu.edu.cn

Citation:

Mei, J., Ma, G., Guo, C., Wu, T., Zhao, J., & Zhou, W. (2025). Deciphering landslide precursors from spatiotemporal ground motion using persistent homology. *Journal of Geophysical Research: Earth Surface*, 130, e2024JF007949. <https://doi.org/10.1029/2024JF007949>

Received 19 JUL 2024

Accepted 21 JAN 2025

Author Contributions:

Conceptualization: Jiangzhou Mei, Gang Ma

Data curation: Jiangzhou Mei, Chengqian Guo, Ting Wu

Formal analysis: Gang Ma, Chengqian Guo, Ting Wu, Jidong Zhao, Wei Zhou

Funding acquisition: Wei Zhou

Investigation: Jiangzhou Mei, Gang Ma, Chengqian Guo, Ting Wu, Jidong Zhao, Wei Zhou

Methodology: Jiangzhou Mei, Gang Ma

Project administration: Gang Ma

Resources: Jidong Zhao

Software: Jiangzhou Mei, Chengqian Guo

Supervision: Gang Ma, Jidong Zhao, Wei Zhou

Validation: Jiangzhou Mei, Gang Ma, Chengqian Guo, Ting Wu, Jidong Zhao, Wei Zhou




Visualization: Jiangzhou Mei, Gang Ma, Chengqian Guo, Ting Wu, Jidong Zhao, Wei Zhou

Writing – original draft: Jiangzhou Mei

Writing – review & editing: Gang Ma, Chengqian Guo, Ting Wu, Jidong Zhao, Wei Zhou

© 2025. American Geophysical Union. All Rights Reserved.

Deciphering Landslide Precursors From Spatiotemporal Ground Motion Using Persistent Homology

Jiangzhou Mei^{1,2,3} , Gang Ma^{1,2,3} , Chengqian Guo^{1,3}, Ting Wu^{1,3}, Jidong Zhao⁴ , and Wei Zhou^{1,2,3}

¹State Key Laboratory of Water Resources Engineering and Management, Wuhan University, Wuhan, China, ²Institute of Water Engineering Sciences, Wuhan University, Wuhan, China, ³Key Laboratory of Rock Mechanics in Hydraulic Structural Engineering of Ministry of Education, Wuhan University, Wuhan, China, ⁴Department of Civil and Environmental Engineering, The Hong Kong University of Science and Technology, Hong Kong, China

Abstract Landslides are major natural disasters that pose significant challenges for prediction. Recent advances in monitoring tools have led to the accumulation of monitoring data with high spatiotemporal resolution, calling for new and robust methodologies to efficiently analyze these complex big data and accurately predict landslides. Here, we present a persistent homology-based method that integrates the slope-scale monitoring data from interferometric synthetic aperture radar with novel measures of spatiotemporal evolution of slope deformation to identify early warning precursors for impending landslides. Our proposed method can capture critical patterns of accelerated deformation evolution and generate warning signals long before the landslide occurrence. Six case studies confirm the effectiveness and accuracy of the proposed method in landslide prediction, with a leading time exceeding 100 days for the Xinmo and Mud Creek landslides. Strong spatiotemporal correlations of slope deformation underscore long-range effective predictions. Our method offers a new, robust alternative to the conventional threshold-based approach for understanding and predicting landslides in natural slopes.

Plain Language Summary Landslides, characterized by sudden runaway slope failures, may cause a lot of damage and put people's lives at risk. We have developed new ways to monitor slopes using technology like interferometric synthetic aperture radar, which can detect small changes in the ground that might indicate a landslide is about to happen. While these methods provide vast monitoring data regarding the spatiotemporal evolution of dangerous slopes, methods that can handle these big data and distill precursory information regarding the upcoming landslides are still lacking. To address this, we proposed a new method that looks at how the slope deformation changes over time. We found that there are patterns of acceleration in the deformation that can indicate a landslide is coming. This method can analyze the monitoring data covering the whole slope and is better than transitional methods that focus only on displacement time series from a single or a small set of monitoring points. This new method could also be useful for other fields that deal with large amounts of complex data. Moreover, the proposed method provides valuable insights into many related fields grappling with explosive data volume and complexity, ranging from climate changes to natural hazards and solar radiation.

1. Introduction

Landslides are among the most destructive natural disasters, causing extensive damage to infrastructure and posing a significant threat to human life and property (Intrieri et al., 2019; Lei et al., 2023; Schönfeldt et al., 2022). Since the relevance between slope creep and precipitation is high (Handwerger et al., 2019, 2022), the ongoing climate changes are likely to increase the occurrence of extreme precipitation events, which will undoubtedly have a profound influence on the global risk of landslides (Gariano & Guzzetti, 2016; Kirschbaum et al., 2020; Picarelli et al., 2021). As a result, monitoring, modeling, and predicting the occurrence of landslides have received considerable attention in recent decades (Casagli et al., 2023; K. T. Chen & Wu, 2018; Fan et al., 2017; Lacroix et al., 2020; Piciullo et al., 2018). While advances in monitoring techniques have provided abundant data for investigating landslides, early warning for upcoming landslides remains a challenging task due to the highly variable nature of slope motion in both space and time (Lei & Sornette, 2023; Poli, 2017). Existing early warning methods typically focus on the deformation time series from individual monitoring points (MPs) and rely on

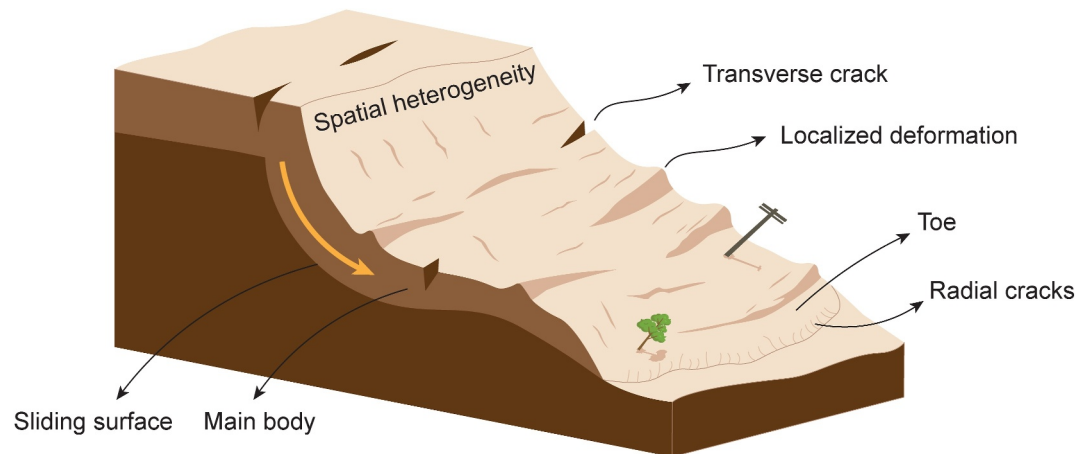


Figure 1. Schematic depiction of the spatial heterogeneity of landslide deformation.

setting some alert thresholds for landslide velocity/acceleration or rainfall intensity (Crosta & Agliardi, 2002; Intrieri et al., 2019; Kothari & Momayez, 2018; Lacroix et al., 2020).

As illustrated in Figure 1, slow-moving landslides exhibit non-uniform spatial and temporal kinematic changes under the coupled influence of heterogeneous geological structures, seasonal rainfall, earthquakes, and human activities (Casagli et al., 2023; Cohen-Waeber et al., 2018; Ding et al., 2023; Lacroix et al., 2020). Given their complexity, landslides manifest in various types of failure such as slides, flows, and falls as well as complex combinations of these, leading to distinct spatial deformation patterns (Hung et al., 2014; Lacroix et al., 2020). Recent studies have demonstrated that the spatial pattern of slope deformation contains critical information related to landslide failure processes, such as landslide kinematic progression, failure depth, sinuosity, compactness, and variations in slope (Bhuyan et al., 2024). Through data-driven methods, these spatial deformation patterns can be quantitatively linked to their triggers and underlying failure types (Bhuyan et al., 2024; Rana et al., 2021).

Moreover, recent research indicates that regions approaching catastrophic failure display different spatiotemporal characteristics from stable ones (Singh & Tordesillas, 2020; S. Zhou et al., 2022). In this context, many spatial analysis techniques, such as community detection (Desai et al., 2023) and outlying aspects mining (S. Zhou et al., 2022), have been proposed to identify potential failure zones within extensive monitoring data sets. Collectively, these studies suggest that the spatiotemporal evolution of landslide deformation provides valuable insights into the underlying failure mechanisms and kinematic processes of landslides. Therefore, it is reasonable to speculate that by investigating the spatiotemporal evolution of landslide deformation, one may uncover kinematic parameters that are capable of revealing early warning signals about impending landslides or even supporting predictions of the timing of failure.

Recent years have witnessed an explosion of monitoring techniques that can examine slope motion with high spatial and temporal resolution (Giri et al., 2019; Jaboyedoff et al., 2012; Kothari & Momayez, 2018; Le Breton et al., 2021). Among those, interferometric synthetic aperture radar (InSAR) has emerged as one of the most promising techniques, providing continuous and large-scale monitoring data at the slope scale (Cohen-Waeber et al., 2018; Rouet-Leduc et al., 2021). As a result, InSAR has been incorporated into the early warning systems (EWS) (Di Traglia et al., 2021; Teshebaeva et al., 2019) to detect occurred and impending landslides (Intrieri et al., 2018; Li et al., 2022). While advancements in remote-sensing techniques allow for monitoring data that cover entire slopes, there is an urgent need for methods that can quantify the spatiotemporal evolution of slope deformation to better anticipate impending landslides (Intrieri et al., 2019; Leinauer et al., 2023; Singh & Tordesillas, 2020).

In this work, we focus on identifying potential landslide precursors through the identification of slope deformation patterns that are indicative of impending catastrophic failure. To achieve this, we propose a persistent homology-based method to quantify the spatiotemporal evolution of slope deformation. We demonstrate how this method can integrate comprehensive slope-scale monitoring data and capture precursory signals before the

occurrence of landslides. We further test our method using InSAR monitoring data from six representative landslides. Finally, we assess the robustness and superiority of the proposed method compared with conventional threshold-based alert methods.

2. Methods

In this work, a persistent homology-based method is proposed to quantify the spatiotemporal evolution of ground deformation at the slope scale. Persistent homology (PH) provides an algebraic topology-based framework to quantify the persistence of topological invariants from multiscale data in Euclidean space or graph-based data. PH can precisely describe the topological characteristics of complex networks by probing their inherent topological structures. In recent years, PH has proven promising in studying the evolution of large data sets with complex spatiotemporal characteristics and has been widely adopted in fields encompassing material science (Hiraoka et al., 2016; Mei et al., 2023), natural language analysis (Zhu, 2013), and biology (Kovacev-Nikolic et al., 2016).

Before a detailed introduction to the persistent homology method, we first introduce tools from network theory to describe the spatial distribution of monitoring points (MPs). For each date, we define a monitoring point network (MPN) to represent the spatial distribution of InSAR monitoring points that have continuous data over the time period of interest. In network theory, a network typically consists of nodes and the edges connecting them, providing a powerful framework to characterize interactions within complex systems (Desai et al., 2023; Papadopoulos et al., 2018). In this study, the MPN is defined solely on the spatial locations of InSAR monitoring points, as indicated in Figure 2a. Specifically, each monitoring point (MP) is treated as a node in the network, and an edge is assigned to connect two monitoring points (nodes) if their spatial distance is less than a specified cutoff distance L_c . Each node is then assigned the velocity of its corresponding monitoring point on the current date. The MPN, along with the velocity information, serves as the foundation for the subsequent persistent homology analysis.

Based on the MPN, the proposed persistent homology method can be described as two parts: the spatial filtration process and distance calculation. Specifically, the former is designed to investigate how topological invariants emerge and disappear with varying filtration thresholds. This process achieves a significant dimension reduction of the original network while maintaining its inherent topological properties. Taking the MPN shown in Figure 2b as a heuristic example, the spatial filtration process is realized by continuously increasing the velocity threshold η . First, given an initial threshold η , a partial monitoring network containing MPs with velocity smaller or equal to this threshold can be obtained. From this partial monitoring network, we can extract a commonly used topological structure called component (Wasserman, 2018). A component is defined as a local maximally connected group of nodes within a given network (Mei et al., 2023). Any two nodes within a component can reach each other via paths but are not connected to any nodes outside this component. Thus, the initial threshold should be sufficiently small to catch the appearance of components with the smallest values of velocity. Then the velocity threshold η is continuously increased and a partial monitoring network at each threshold is also defined. In this way, we can obtain a sequence of partial monitoring networks and track the appearance and death of each component. The death of a component refers to its mergence with another component that appeared earlier. As shown in Figure 2b, components are referred to as $C-k$, where k is the order of appearance during the spatial filtration process. For example, $C-1$ refers to the first appeared component and appears when the threshold η increases to $-v_1$. The component $C-2$ appears at $\eta = -v_2$ and merges with $C-1$ when η further increases to $-v_3$. Given that $C-1$ appears earlier than $C-2$ during the filtration process, the persistence of $C-2$ refers to the interval between $-v_2$ and $-v_3$.

Persistent diagrams (PD) are then employed to illustrate the results of the spatial filtration process. Specifically, a persistent diagram is the representation of points that encode the information about the appearance and disappearance of components during the spatial filtration process. As indicated in Figure 2c, for a chosen point $(\eta_{\text{birth}}; \eta_{\text{death}})$ in the persistent diagram, η_{birth} and η_{death} correspond to the velocity thresholds at which the corresponding component appears (birth) and merges with others (death), respectively. Therefore, each point in the persistent diagram provides essential information regarding the existence of a component over the spatial filtration process. In short, the spatial filtration process employs a multi-scale analysis to examine the hierarchical structure of complex networks, and the resulting persistent diagram achieves significant dimension reduction of the ground deformation field by encoding its inherent topological features.

After the spatial filtration process, the spatiotemporal evolution of slope deformation can be represented by the time-varying persistent diagrams. We further calculate the distance between two temporally adjacent persistent

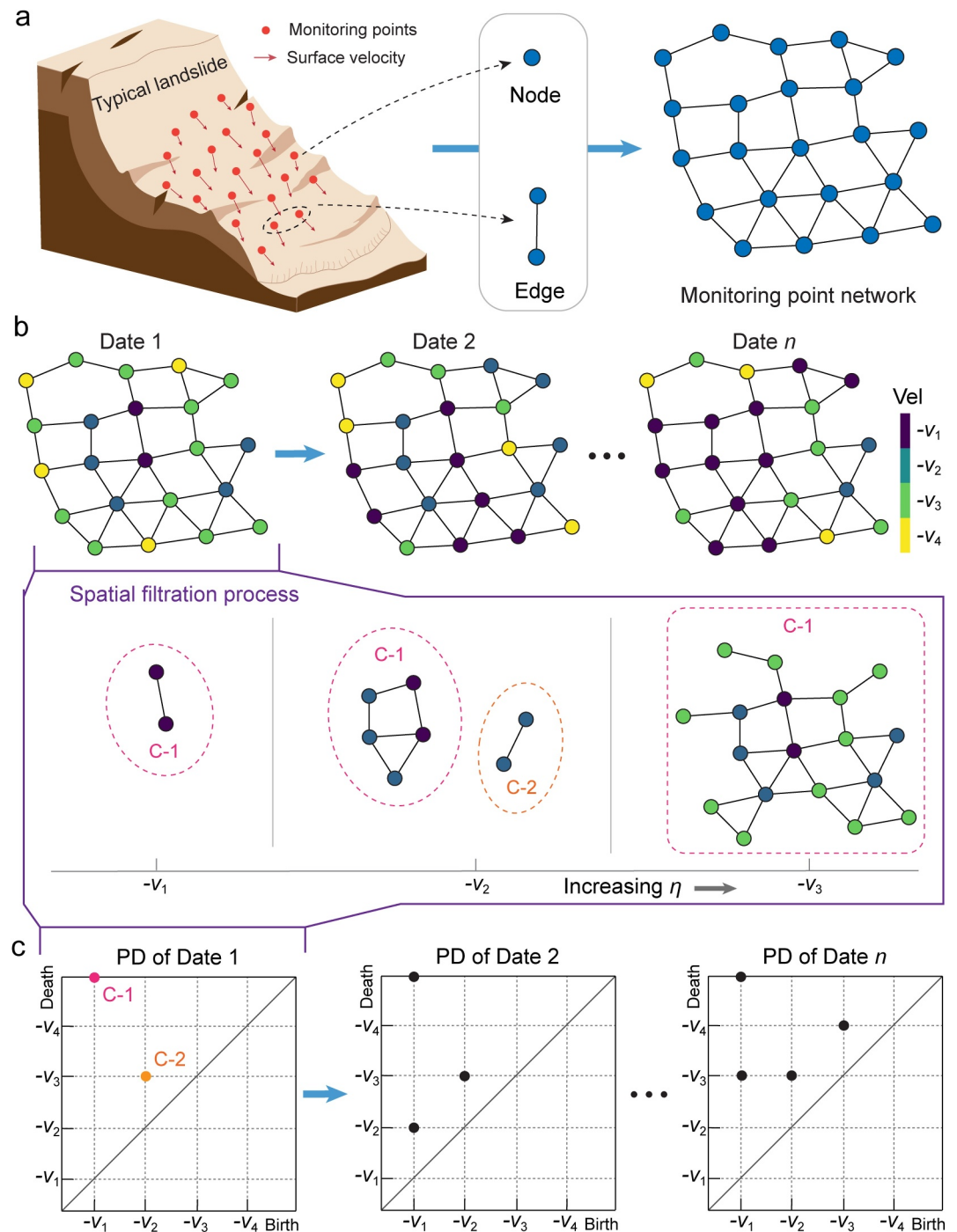


Figure 2. Methodology of persistent homology. (a) Schematic of a monitoring point network (MPN) constructed from discretely distributed monitoring points. (b) Spatial filtration process by continuously increasing velocity threshold η . Each point is colored by its moving velocity. The shown spatial infiltration example is only for one time slice of the MPN. (c) Persistent diagrams that encode the birth and death information of components.

diagrams to quantify its evolution. The Wasserstein distance is among the most commonly used distance metrics and is adopted in this study. Given two temporally adjacent persistent diagrams PD_s and PD_t , their Wasserstein distance $\Delta WD_{s,t}$ can be calculated as

$$\Delta WD_{s,t}(PD_s, PD_t) = \min_{\phi(PD_s, PD_t)} \left(\sum_{p \in PD_s} d(p, \phi(p))^2 \right)^{1/2} \quad (1)$$

where PD_s and PD_t are persistent diagrams generated at date s and t ($t > s$), respectively. p iterates over all points in PD_s , and $\phi(p)$ refers to the corresponding point in PD_t via the bijection ϕ . $d(p, \phi(p))$ is the distance between two points and is calculated as

$$d(p, \phi(p)) = \max(|\eta_{\text{birth},p} - \eta_{\text{birth},\phi(p)}|, |\eta_{\text{death},p} - \eta_{\text{death},\phi(p)}|) \quad (2)$$

Thus, the Wasserstein distance is dependent on the choice of ϕ , and the final result is determined as the minimum value over all possible bijections. Then we define the cumulative Wasserstein distance at date t as

$$WD_t = WD_s + \Delta WD_{s,t} \quad (3)$$

By definition, the slope of WD curve indicates the intensity of topological properties evolution and essentially reflects the spatiotemporal evolution rate of slope deformation. Taken together, the proposed PH method consists of two parts: spatial filtration process and distance calculation. The former aims to determine the spatial distribution of moving velocities and how points with different velocities relate across the slope, reflecting the spatial structure of the slope deformation field. The distance calculation part investigates how this spatial structure changes over time. The resulting temporal evolution of WD serves as a quantitative indicator of the spatiotemporal evolution rate of slope deformation.

3. Results

In this work, we employ the proposed persistent homology (PH) method to quantify the spatiotemporal evolution of slope deformation and identify landslide precursors from the InSAR monitoring data. We resort to the Sentinel-1A/B satellite to obtain SAR images with a spatial resolution of 15 m, which are further processed using the SBAS-InSAR technique (Berardino et al., 2002; Li et al., 2022). By setting appropriate spatial and temporal baselines for SAR images, the SBAS-InSAR technique forms differential interferograms and increases the correlation of interferograms' formation. It is worth noting that the InSAR results of the work are processed using the open-source software SNAP and STAMP. Moreover, atmospheric correction is made via the Generic Atmospheric Correction Online Service for InSAR (GACOS) (Yu et al., 2018). More details about the InSAR processing procedures can be found in our previous study (C. Guo et al., 2022). In this section, we present six landslide cases: three that resulted in catastrophic failure and three that exhibited slow-moving behavior without catastrophic failure.

3.1. Landslide Cases Demonstrating Catastrophic Failures

3.1.1. Xinmo Landslide

The Xinmo landslide that demonstrates catastrophic failure is first examined. On 24 June 2017, the Xinmo landslide, classified as a rock avalanche, devastated Xinmo village in Sichuan Province, southwestern China, as depicted in Figure 3a. The landslide zone is located in the Longmenshan-Minshan Fault zones, which have experienced multiple significant earthquakes in history, including the 1933 Diexi earthquake, the 1976 Songpan-Pingwu earthquake, and the 2008 Wenchuan earthquake. The local climate is shaped by the Westerlies, Asian monsoon, and Tibetan Plateau monsoon, with an annual precipitation averaging 491 mm. Over 70% of precipitation falls between June and September. The landslide zone experienced intense and prolonged rainfall prior to the occurrence of the Xinmo landslide. Previous studies indicate that the Xinmo landslide was initiated by the failure of a rock mass, which had been already weakened by the 1933 Diexi earthquake (Fan et al., 2017). The combined impact of seismic activity and rainfall is considered a key factor in triggering the landslide (Intrieri et al., 2018; Moretto et al., 2021). This event has been widely regarded as one of the most catastrophic landslides in recent years, and more details are available in many existing studies (Intrieri et al., 2018; S. Zhou et al., 2022).

We utilize the Sentinel-1A/B satellite to obtain 45 SAR images spanning from 9 October 2014 to 19 June 2017, that is, 5 days before the failure. These SAR images cover the entire area of Xinmo village and Songping gully and

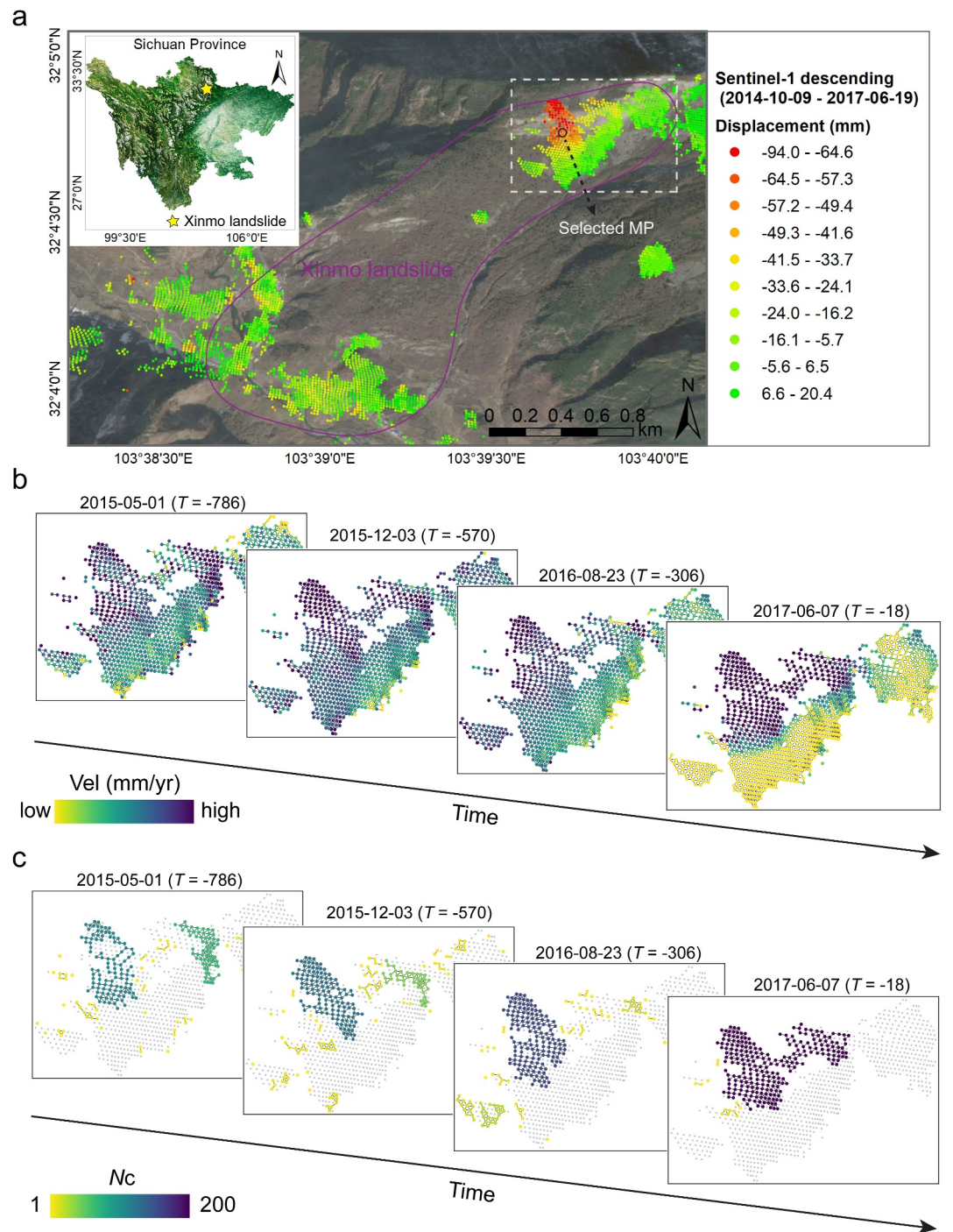


Figure 3. Collective motion toward catastrophic failure. (a) Ground displacement map (from 9 October 2014 to 19 June 2017) of the Xinmo landslide, with inset showing its location within the Sichuan Province of China. The selected MP is used in the analysis in Figure 12. (b) Deformation velocity map at four typical time points, that is, $T = -786$, $T = -570$, $T = -306$, and $T = -18$. T refers to the days before the ultimate failure, and $T = 0$ means the occurrence of landslide. (c) Evolution of the spatial distribution of highly mobile clusters. Each cluster is colored according to its size N_c , which is defined as the number of MPs it contains.

are acquired along the descending orbit and processed using the SBAS-InSAR technique (Berardino et al., 2002; Li et al., 2022). Figure 3a shows the pre-event displacement map (ranging from 9 October 2014 to 19 June 2017) of the Xinmo landslide. Positive values correspond to motion toward the SAR satellite, while negative values

correspond to deformation away from the satellite. Following the procedures described above, we construct a network to describe the spatial distribution of MPs. Specifically, we treat each MP as a node and assign an edge between two adjacent MPs. Two MPs are considered adjacent if their spatial distance is less than a cutoff distance L_c . We note that, unless otherwise specified, the results presented in this study are based on $L_c = 20$ m, and we will demonstrate later different choices of L_c have minimal impact on our conclusions.

We first examine the temporal evolution of slope deformation from a network-based perspective. Figure 3b illustrates the deformation velocity map at four typical dates. Long before the landslide occurs, the velocity map exhibits a less concentrated spatial distribution while showing a sharp transition to collective motion near the occurrence of the landslide. The collective motion indicates the formation of highly mobile clusters in space and can be quantified via clustering analysis. This method is widely utilized in the geoscience and material science communities with the purpose of identifying patterns and spatial correlations among highly mobile sites (Desai et al., 2023; Ghosh et al., 2017; Kou et al., 2018). Previous studies commonly use thresholds between 10% and 25% to select these sites (Li et al., 2021; Mei et al., 2025). Accordingly, we focus on MPs within the MPN that fall within the top 25% of the highest deformation velocities, defining these as highly mobile sites. These points are then used to construct a partial MPN. Clusters within this network are identified, with each cluster defined as a locally connected group of nodes. Therefore, a cluster is the same as the component in the persistent homology method. As shown in Figure 3c, we observe the enlargement of highly mobile clusters when approaching the ultimate failure, which serves as compelling indicators of an intensified spatial correlation within the ground deformation map accompanied by the conspicuous emergence of collective motions. This underscores the imperative need to quantify the spatiotemporal evolution of slope deformation, which may hold the potential of unveiling precursory signals of impending landslides.

The above analysis suggests that quantifying the spatiotemporal evolution of slope deformation can provide enhanced insights into the early signs of impending landslides. Therefore, the persistent homology method is further employed to quantify the spatiotemporal evolution of ground deformation at the slope scale. Figures 4a and 4b show the spatial filtration process and the resulting persistent diagram for a typical ground deformation map of the Xinmo landslide. The evolution of persistent diagrams can be quantified by the Wasserstein distance (see Section 2 for details). Figure 4c shows the evolution of cumulative Wasserstein distance WD with the approaching of the Xinmo landslide. As we have mentioned, the slope of WD curve indicates the intensity of topological properties evolution and essentially reflects the spatiotemporal evolution rate of landslide deformation.

As indicated in Figure 4c, WD shows a typical two-stage evolution trend that increases slightly at the initial stage (blue-shaded region) with a rapid increase afterward (red-shaded region). The former indicates a steady evolution behavior of the slope deformation, which may correspond to the initial and secondary creep stages of the traditional three-phase creep behavior (Noda & Chang, 2023). The latter stage is accompanied by the sudden acceleration of the evolution of ground deformation. Recalling the above analysis, this behavior essentially indicates the emergence of some precursory spatiotemporal motions before the ultimate failure. From the perspective of soft matter physics, it can be regarded as the slope entering into a marginally stable state, delicately poised on the verge of instability (Baule et al., 2018; Deshpande et al., 2021). In this state, the slope becomes fragile and is susceptible to catastrophic failures triggered by some external factors, such as heavy rainfalls (Handwerker et al., 2022; Iverson, 2000; Notti et al., 2021) and earthquakes (Bell, 2018; Yin et al., 2009; Zhao et al., 2023). Thus, the transition point between these two stages acts as a precursory indicator of the impending landslide.

Identifying transition points in the evolution of WD is closely related to the longstanding topic of online (or real-time) changepoint detection within time series data (Goswami et al., 2018). Unlike offline algorithms, which identify transition points by analyzing the entire data set retrospectively, online algorithms work concurrently with data collection, processing each data point as it arrives to detect changes as quickly as possible (Aminikhanghahi & Cook, 2017). Efficient online changepoint detection algorithms include the Bayesian-based (Ruggieri & Antonellis, 2016), kernel-based (Ferrari et al., 2023), and machine learning methods (Zhang & Shi, 2020), which typically require large amounts of data to calculate probability distributions or to train models (Aminikhanghahi & Cook, 2017; Lei et al., 2023). This need for high data volume makes them currently unsuitable for the InSAR data used in this study. Therefore, we introduce a 3σ criterion to identify the transition point from the evolution of WD, which is a traditional heuristic approach presuming that most values lie within

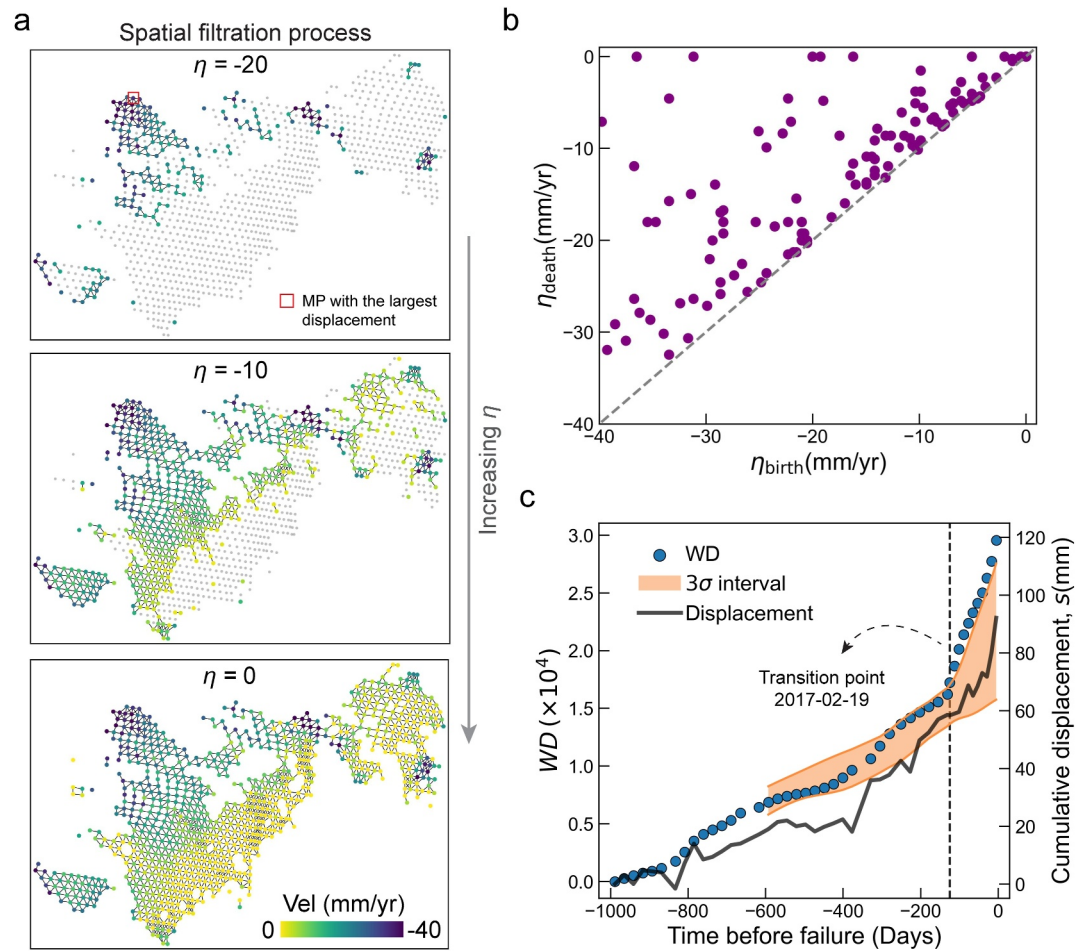


Figure 4. Persistent homology reveals landslide precursors. (a) Typical spatial filtration process of ground deformation map with the increasing of velocity threshold η . The red square highlights the MP with the largest cumulative displacement throughout the study period. (b) Resulting persistent diagram after the spatial filtration process. (c) Evolution of the cumulative Wasserstein distance WD with the approaching of landslide. The black line shows the maximum cumulative displacement within the Xinmo landslide zone, and the corresponding MP is shown by the red square in panel (a).

three standard deviations of the mean. This criterion is straightforward to implement and has been widely used for anomaly detection in time series data (Cui et al., 2019; Liu et al., 2023). With future monitoring data at much higher temporal resolution, further improvements of the proposed PH method can benefit from the aforementioned state-of-the-art detection algorithms.

The 3σ criterion can be briefly described as follows. At each date i , we use a linear function to fit the data from WD_0 to WD_i , from which we can get the standard deviation σ between the predicted values and real values. Moreover, by extending the fitting, we can get the estimated value at the next date, WD'_{i+1} . If the real value at the next date, WD_{i+1} , falls within the range of $WD'_{i+1} \pm 3\sigma$, WD_{i+1} is considered reasonable, and no transition point is identified. However, if WD_{i+1} falls outside this range, a transitional point indicative of the landslide precursor is recognized. To account for the seasonal deformation behaviors of landslides, the first year of WD serves as the baseline for calculating the 3σ interval, and WD_i begins from the second year. Through this criterion, it is demonstrated that the Xinmo landslide exhibits a failure precursor about 125 days prior to its occurrence (see the dotted line in Figure 4c). Moreover, Figure 5 shows the evolution of WD calculated based on different L_c , where the trend of WD and resulting failure precursors are independent of different choices of L_c . We note the decreasing of WD with increasing L_c is due to the fact that a smaller value of L_c exhibits more isolated components, which further increases the calculated Wasserstein distance between two persistent diagrams.

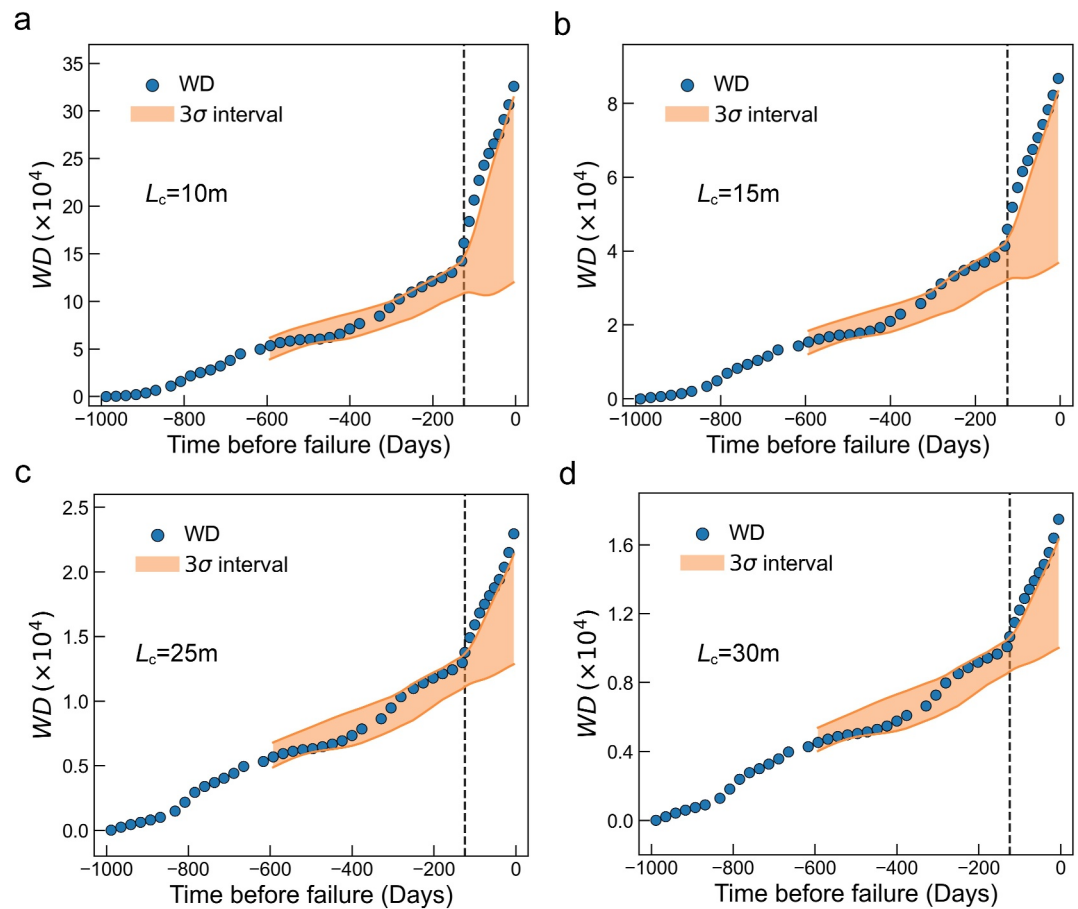


Figure 5. Evolution of WD calculated based on different choices of L_c : (a) $L_c = 10$ m, (b) $L_c = 15$ m, (c) $L_c = 25$ m, and (d) $L_c = 30$ m. Dotted lines denote the early warning dates detected by the 3σ criteria.

3.1.2. Mud Creek Landslide

The proposed PH method is further employed to verify its applicability for a second case, the Mud Creek landslide. On 20 May 2017, the Mud Creek landslide occurred in California, United States (see Figure 6a), destroying part of California State Highway 1 (CA-1). The landslide zone is located in the California Coast Ranges, where slow-moving landslides are prevalent due to mechanically weak rocks, active uplift, and high seasonal precipitation (Desai et al., 2023). Annual precipitation averages around 1,000 mm, with 80% occurring between October and May (Desai et al., 2023). It is worth noting that this region experienced a historic drought that lasted from 2012 to 2016, followed by the wettest year (2017) on record. As indicated in a previous study, the Mud Creek landslide demonstrated decades of creep behavior before its failure and is believed to be triggered by increased pore-fluid pressure from heavy rainfall (Handwerker et al., 2019). More details can be found in previous studies (Desai et al., 2023; Urgilez Vinueza et al., 2022).

We obtain 59 SAR images along the descending orbit that span from 12 May 2015 to 13 May 2017, that is, 7 days before the failure. Similarly, we obtain the ground deformation map from these SAR images through the SBAS-InSAR technique. Figure 6b illustrates the pre-failure displacement map (from 12 May 2015 to 13 May 2017) of the Mud Creek landslide, in which we show the outline of the Mud Creek landslide. Following the above procedures, we quantify the spatiotemporal evolution of the deformation field of the Mud Creek landslide. The resulting evolution of WD also demonstrates a two-stage evolution trend, as shown in Figure 6c, with surprising similarity with that of the Xinmo landslide. Through the proposed 3σ criterion, our method generates failure precursors identifiable about 127 days prior to the occurrence of the Mud Creek landslide. In comparison to the maximum cumulative displacement within the landslide zone (see Figure 6c), our method surely generates a much clearer signal for the impending catastrophic failure.

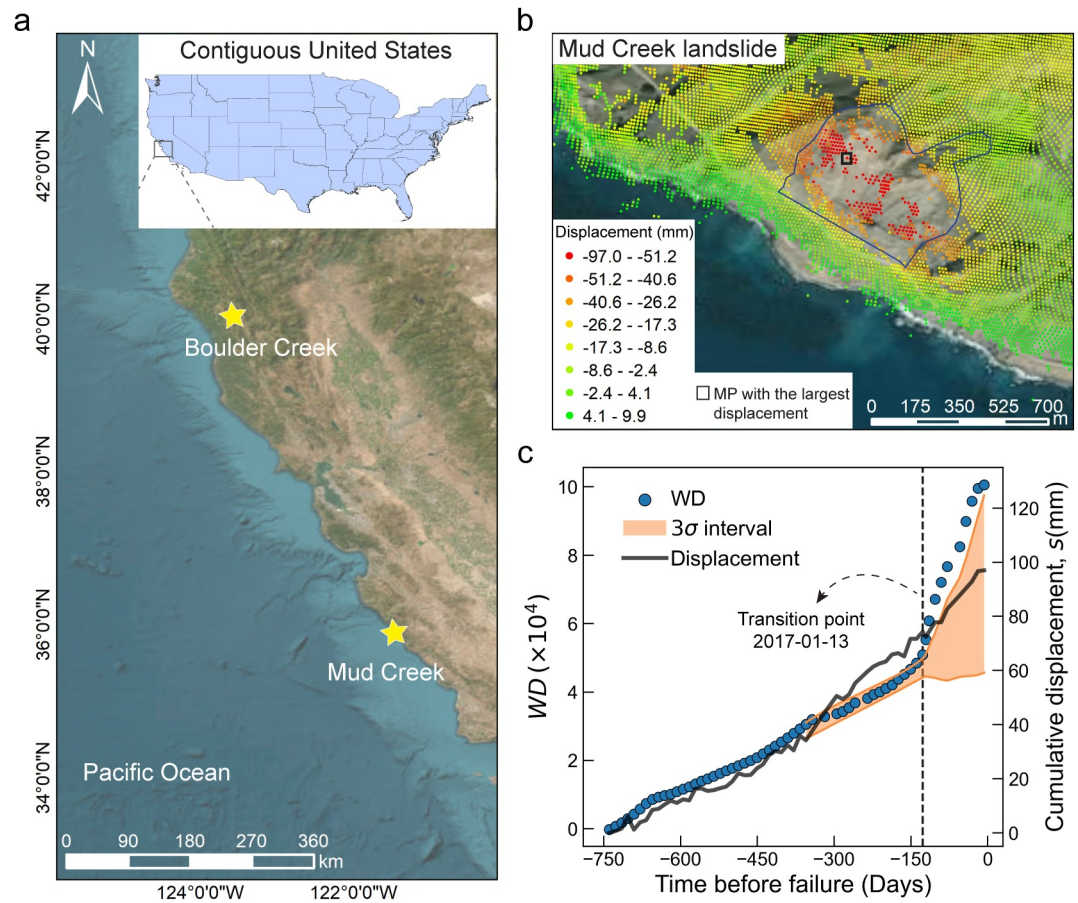


Figure 6. Precursory analysis of the Mud Creek landslide. (a) Geographic location of Mud Creek landslide within United States. (b) Pre-failure displacement map (from 12 May 2015 to 13 May 2017) of Mud Creek slope captured by interferometric synthetic aperture radar monitoring. (c) Evolution of WD with the approaching of Mud Creek landslide. The black line shows the maximum cumulative displacement within the Mud Creek landslide zone, and the corresponding MP is highlighted by the black square in panel (b).

3.1.3. Longjing Landslide

To further validate the effectiveness of the proposed method, we applied it to the Longjing landslide, which has different failure conditions than the previously analyzed sites. The Longjing landslide occurred on 19 February 2019, in Guizhou Province, China. The landslide zone is generally dominated by karst topography and a subtropical monsoon climate. The region receives over 1,300 mm of annual precipitation, mostly between May and October. The landslide material comprises thick-bedded dolomite that slides along weak bedrock layers rich in argillaceous limestone and dolomite. Unlike the aforementioned two catastrophic landslides, the Longjing landslide was triggered by slope toe excavation (Fan et al., 2019; Zeng et al., 2024). Using Sentinel-1A/B satellite data, we obtained 58 SAR images from 20 March 2017 to 14 February 2019 (5 days before failure) along the ascending orbit. Figures 7a and 7b show the resulting displacement map and the evolution of WD, respectively. The results show that the proposed method identifies the early warning signal on 9 January 2019, that is, 41 days ahead of the occurrence of the Longjing landslide. This demonstrates that our method can effectively apply to a wider range of natural landslides under different failure conditions.

3.2. Slow-Moving Landslides Without Catastrophic Failure

The aforementioned cases represent landslides that have undergone catastrophic failure. In the following section, we apply our method to three slow-moving landslides that exhibit continuous creeping behavior but have not eventually undergone catastrophic failure, namely the Cheyiping landslide, Zhenggang landslide, and Boulder Creek landslide.

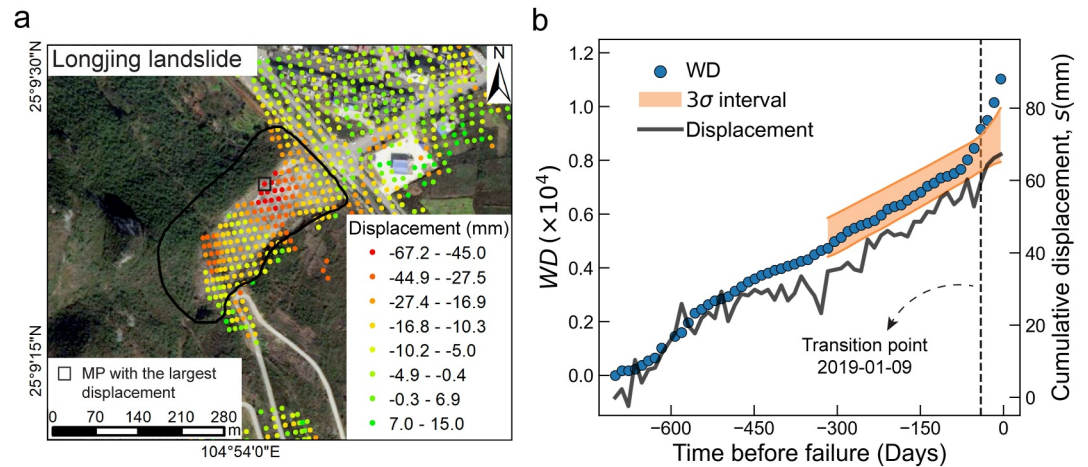


Figure 7. The precursory analysis of Longjing landslide. (a) Pre-failure displacement map of the Longjing landslide from 20 March 2017 to 14 February 2019. (b) Evolution of WD with the approaching of Longjing landslide. The black line shows the maximum cumulative displacement within the landslide zone, and the corresponding MP is highlighted by the black square in panel (a).

3.2.1. Cheyiping and Zhenggang Landslides

As shown in Figures 8a and 9a, the Cheyiping and Zhenggang landslides are both located in the Yunnan province of China. The region is characterized by high mountains and deep valleys formed by the uplift of the Tibetan Plateau due to the collision between the Indian and Asian plates. The local climate is classified as a subtropical plateau monsoon climate, with over 85% of annual precipitation occurring between May and October. The Cheyiping landslide is situated in the upper reaches of the Lancang River in Lanping County, approximately 39 km from the Huangdeng Hydropower Station. It is a typical reactivated reservoir landslide, with materials primarily consisting of Quaternary deposits of silty clay and fragmented rubble. The underlying bedrock comprises silty mudstone, argillaceous siltstone, and sandstone from the Middle Jurassic Huakaizuo Formation. The Zhenggang landslide, located downstream on the right bank of the Lancang River, comprises quaternary deposits, including residual slope sediments and collapse materials. The underlying bedrock primarily consists of sandstone and slate. Further details about these two landslides are available in previous studies (Chong et al., 2016; C. Guo et al., 2022).

For the Cheyiping landslide, 114 InSAR images that span from 6 November 2017 to 10 September 2021 are obtained along the ascending orbit. Similarly, for the Zhenggang landslide, 75 SAR images spanning from 23 April 2017 to 8 February 2022 are obtained along the ascending orbit. Figures 8b and 9b show the ground displacement maps over the investigated periods for Cheyiping and Zhenggang landslides, respectively. As depicted in Figures 8c and 9c, the maximum cumulative displacements of these landslides exhibit similar continuous creeping behavior, albeit with significant fluctuations. Following the same procedure, we test the proposed persistent homology method on these two landslides, and the resulting WD series are respectively shown in Figures 8d and 9d. It is important to note that Yunnan Province in southwest China experiences high precipitation (Huang, 2009), which surely has a profound influence on the spatiotemporal evolution of landslide movement (Gariano & Guzzetti, 2016; Paul et al., 2024; Sreejith et al., 2024). To illustrate the relationship between precipitation and landslide deformation, we have included monthly rainfall data in these figures, represented by the blue bars at the bottom. It is shown that WD exhibits a nearly linear evolution for both landslides and no transition point is detected via the 3σ criterion. Recalling the results of the above sites with catastrophic failures, we demonstrate the effectiveness of our method in quantifying the spatiotemporal evolution of slope deformation patterns and detecting landslide precursors.

Furthermore, for the Zhenggang landslide, high levels of precipitation broadly coincide with accelerated WD evolution, indicating that the proposed method may be effective in analyzing how the spatiotemporal evolution of a landslide is driven by external factors such as precipitation, earthquakes, and groundwater fluctuations. These factors have been shown to significantly alter the hydro-mechanical properties of geotechnical materials and affect the movement of large landslides (Handwerger et al., 2019, 2022; Kirschbaum et al., 2020; Ye et al., 2024;

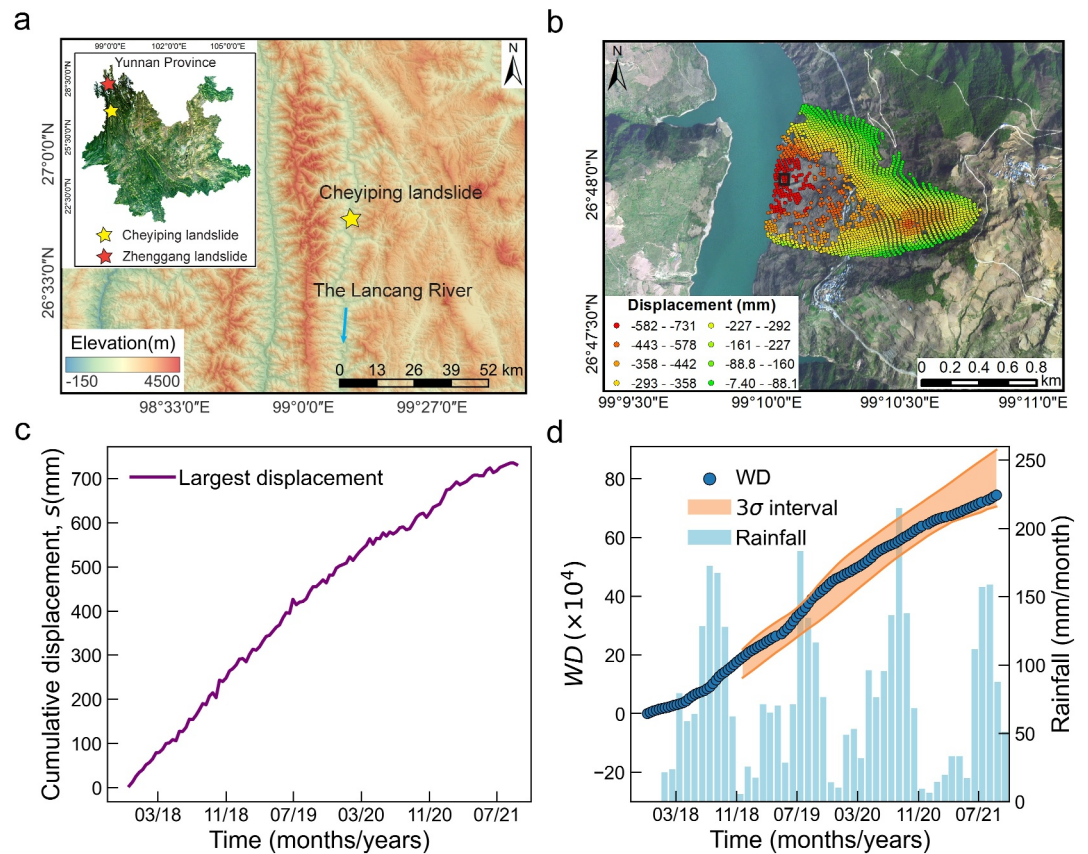


Figure 8. Persistent homology analysis of the Cheyiping landslide, which demonstrates continuous creeping without catastrophic failure. (a) Geomorphic features of the Cheyiping landslide. Inset shows the locations of Cheyiping and Zhenggang landslides within Yunnan Province, China. (b) Ground displacement map of the Cheyiping landslide from 6 November 2017 to 10 September 2021. (c) The maximum cumulative displacement within the landslide zone, and the corresponding MP is highlighted by the black square in panel (b). (d) Evolution of WD and the monthly rainfall.

Zhao et al., 2023). In this context, future research into this topic requires not only deformation monitoring data with higher temporal resolution than currently feasible, but also additional information regarding the mechanical processes such as direct measurements of hydraulic conductivity and pore-fluid pressure at the sliding surface (Finnegan et al., 2022; Murphy et al., 2022; Oya et al., 2024), continuous seismic and acoustic signals (Le Breton et al., 2021; Hu et al., 2018; Q. Zhou et al., 2024).

3.2.2. Boulder Creek Landslide

To further evaluate the effectiveness of the proposed method, we apply it to the Boulder Creek landslide, a site that experienced unprecedented acceleration but did not result in collapse. Both the Boulder Creek and Mud Creek landslides are located within the California Coast Ranges, with further details about the region provided in the description of the Mud Creek landslide. Both sites underwent accelerated deformation from October 2016 to January 2017 due to the shift from historic drought to extreme rainfall (Handwerger et al., 2019); however, unlike Mud Creek, the Boulder Creek landslide ultimately stabilized without collapsing. We obtain 38 SAR images along the descending orbit from 10 June 2015 to 18 May 2017, with the corresponding displacement map of the Boulder Creek landslide shown in Figure 10a. Then, the proposed PH method is adopted to calculate the evolution of WD for Boulder Creek landslide. As illustrated in Figure 10b, a sharp increase in WD occurs around January 2017. The red dashed zone in Figure 10b indicates WD slightly exceeds the 3σ interval near January 2017, which indicates that the Boulder Creek landslide had a strong potential for catastrophic failure at that time. This aligns with prior observations of a transition from historic drought to extreme rainfall in the region during that period (Handwerger et al., 2019). Moreover, after February 2017, WD evolves back into the 3σ interval, aligning with observations that the slope did not collapse but instead continued to deform gradually.

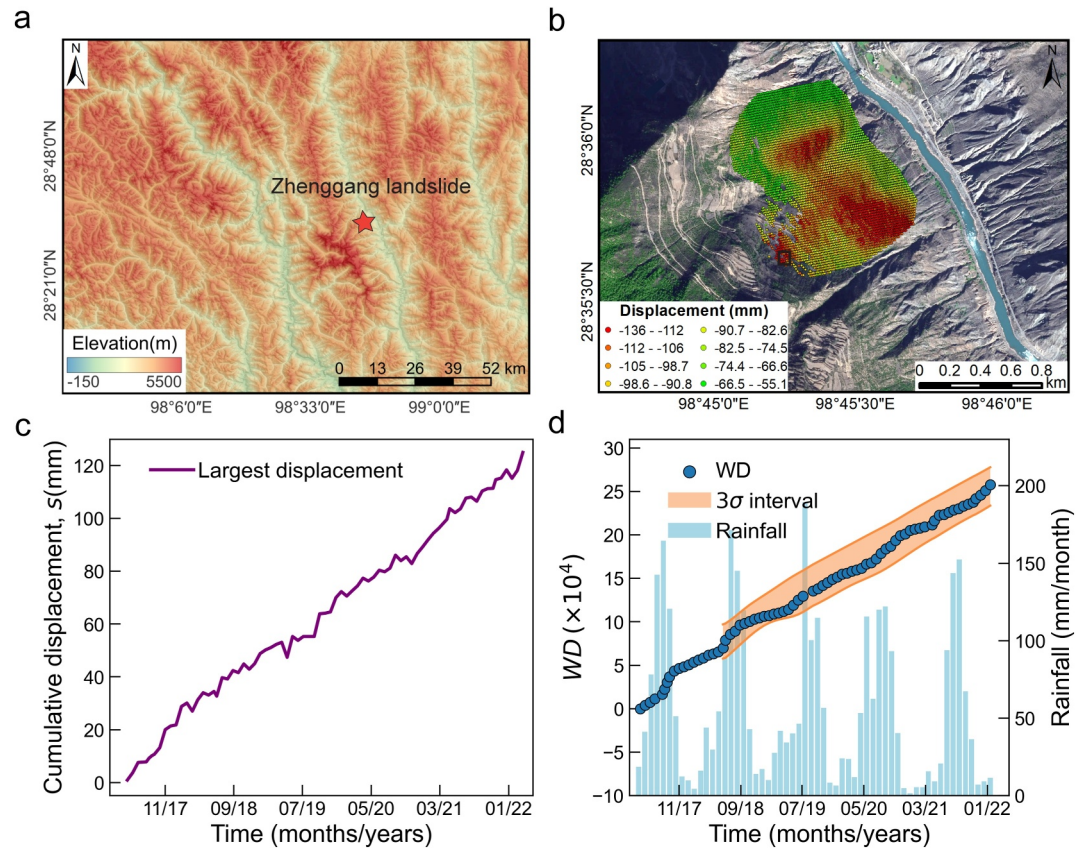


Figure 9. Persistent homology analysis of the Zhenggang landslide, which demonstrates continuous creeping without catastrophic failure. (a) Geomorphic features of the Zhenggang landslide. The location of Zhenggang landslide can be found in Figure 8a (b) Ground displacement map of Zhenggang landslide from 23 April 2017 to 8 February 2022. (c) The maximum cumulative displacement within the landslide zone, and the corresponding MP is highlighted by the black square in panel (b). (d) Evolution of WD and the monthly rainfall.

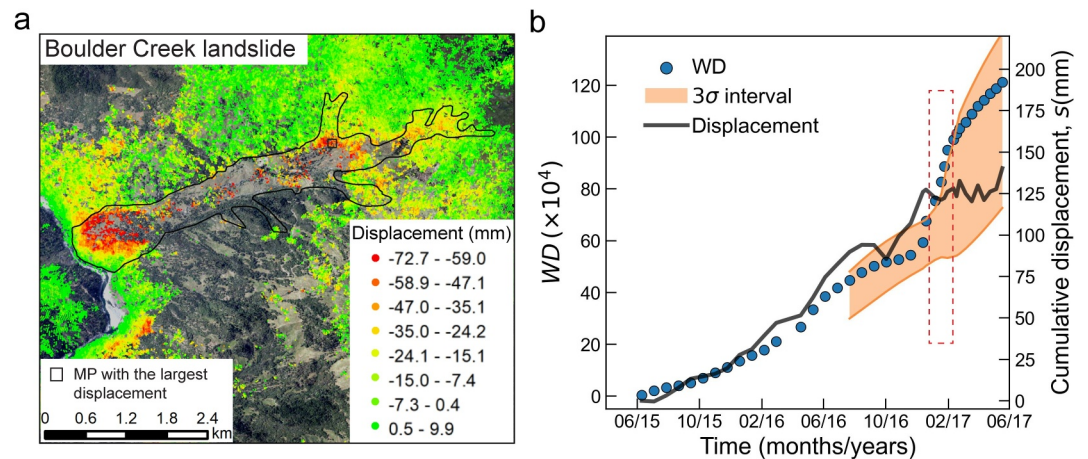


Figure 10. Persistent homology analysis of the Boulder Creek landslide. (a) Ground displacement map of Boulder Creek landslide from 10 June 2015 to 18 May 2017. (b) Evolution of the resulting WD. The red dashed zone indicates the points that exceed the 3σ interval. The black line shows the maximum cumulative displacement within the landslide zone, and the corresponding MP is highlighted by the black square in panel (a).

The results suggest that, while the proposed method robustly identifies landslide precursors through spatio-temporal analysis of slope deformation, it may generate false alerts for landslides undergoing rapid, unprecedented acceleration due to natural variations such as extreme rainfall. This is a common challenge for landslide alert methods that rely solely on surface deformation data (Intrieri et al., 2019; Lei et al., 2023; Leinauer et al., 2023). Previous studies indicate that the catastrophic failure of the Mud Creek landslide was most likely due to frictional weakening caused by a substantial increase in pore-fluid pressure (Handwerger et al., 2019). In contrast, the Boulder Creek landslide was able to adjust to the elevated pore-fluid pressures and maintain stable sliding without failure. These differences are fundamentally related to factors such as the landslide geometry, material properties (such as porosity and rate-strengthening/weakening properties), and drainage networks (Teshebaeva et al., 2019; Youssef & Pourghasemi, 2021). For example, the slope angle and associated gravitational driving stress were lower for the Boulder Creek landslide, reducing the likelihood of catastrophic failure (Handwerger et al., 2019).

Given that landslide movement is controlled by frictional processes along the sliding surface, variations in internal hydro-mechanical properties can significantly alter its frictional resistance (Handwerger et al., 2019; Noda & Chang, 2023). In this context, integrating surface deformation data with internal mechanical information holds promise for minimizing false alerts and enhancing landslide risk management (Le Breton et al., 2021; Oya et al., 2024). However, obtaining in situ information in mountainous or inaccessible areas poses significant challenges (Fan et al., 2017), and the high cost of in situ monitoring sensors makes it impossible for implementation on all possible landslides (Zeng et al., 2024).

For landslide cases where in situ mechanical information is unfeasible, another improvement of the proposed PH method can be made by incorporating additional information into the construction of the MPN. For instance, slope angles and other geometric characteristics between nearby nodes (monitoring points) can be encoded as feature vectors on their connecting edges (Desai et al., 2023). Additionally, material properties can be integrated by assigning different weights to each node based on their local conditions (Papadopoulos et al., 2018). In this way, we can enrich the MPN with more detailed information about slow-moving landslides, enabling a more accurate assessment of the spatiotemporal evolution of slope deformation and potentially reducing false alerts for impending landslides.

4. Discussion

4.1. Comparison With Conventional Early Warning Methods

In this section, using the monitoring data from the Xinmo landslide, we compare the early warning results of the proposed method with those of conventional early warning methods. Generally, conventional alert methods mainly rely on setting alert thresholds for individual displacement time series. To demonstrate the superiority of the proposed method, a comparative analysis is further conducted with two conventional threshold-based alert methods (M. Chen & Jiang, 2020; Xu et al., 2011), that is, the tangential angle-based (TA-based) and velocity and acceleration-based (VA-based) method. The TA-based method focuses on the tangential angle of the displacement curve (Xu et al., 2011). To overcome the question that units of the coordinates of the displacement-time curve may have different dimensions and scales, a previous study proposed a modified tangential angle by normalizing the displacement with the velocity of the stable creep stage. The modified tangential angle of time t_i can be calculated as

$$\alpha_i = \arctan \frac{B(i) - B(i-1)}{t_i - t_{i-1}} \quad (4)$$

where α_i is the modified tangential angle, and $B(i)$ is the normalized displacement with the same dimension and unit with time and can be calculated as

$$B(i) = \frac{S(i)}{v_0} \quad (5)$$

where $S(i)$ refers to the cumulative displacement of time t_i , v_0 is the average velocity of the stable creep stage. In this way, the tangential angle α_i is independent of different units of time, and previous studies have established

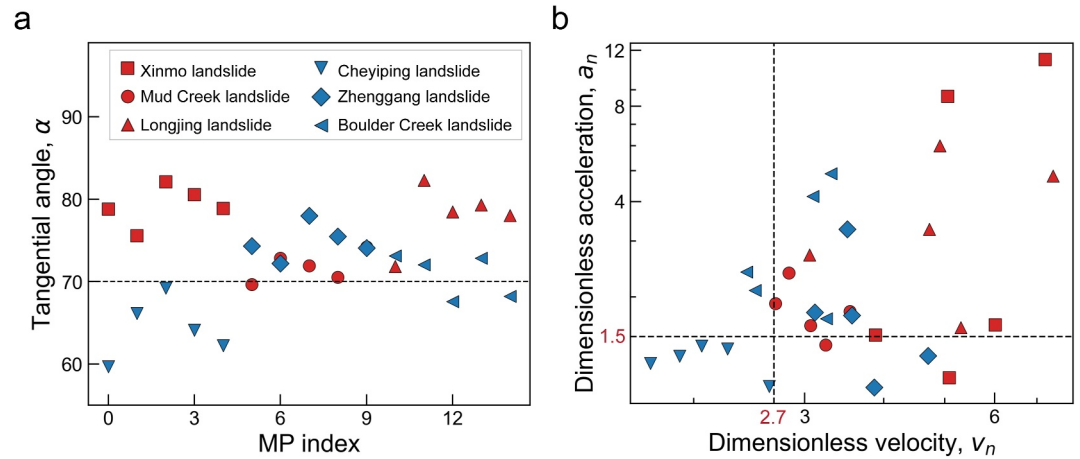


Figure 11. Determining the thresholds for conventional alarm methods. (a) Distribution of the peak value of tangential angle α for different landslides. (b) Distribution of the peak values of dimensionless velocity v_n and acceleration a_n for different landslides. The dashed lines indicate thresholds for conventional alarm methods. Red symbols represent landslides with catastrophic failure, while blue symbols represent landslides without catastrophic failure.

alert thresholds for the tangential angle between values of 80° and 90° (Fan et al., 2019; Intrieri et al., 2019; Xu et al., 2011). For the VA-based method, Chen and Jiang (2020) developed an alert threshold by analyzing 50 landslide failure cases and 50 non-failure cases, using the dimensionless velocity v_n and acceleration a_n :

$$v_n = \frac{v}{v_0}, a_n = \frac{a}{a_0} \quad (6)$$

where a_0 is the initial acceleration of the tertiary/accelerating creep stage. For the non-failure landslide cases, a_0 is selected as the largest acceleration during the first year of study. They found a combination of $v_n = 7$ and $a_n = 4$ can effectively distinguish failed landslides from stable cases and acts as the alert threshold (M. Chen & Jiang, 2020). Therefore, the velocity and acceleration thresholds should be met simultaneously when used for early warning analysis.

However, these thresholds were originally developed using in situ monitoring data, such as the global navigation satellite system and crack gauges, which exhibit much higher temporal resolution than InSAR monitoring data (M. Chen & Jiang, 2020; Fan et al., 2019; Ju et al., 2020). Applying these thresholds directly to InSAR data would fail to generate effective alert signals. Therefore, we further included an analysis on determining reasonable thresholds for these conventional methods. A reliable threshold should effectively differentiate between landslides that result in catastrophic failures and those that do not. According to previous studies (Chen & Jiang, 2020), we selected five monitoring points with the largest displacements from each landslide and calculated the peak values of tangential angle, velocity, and acceleration for each monitoring point throughout the study period. Figure 11a illustrates the distribution of peak values for tangential angles across different landslides. As indicated by the dashed line, the threshold of $\alpha = 70^\circ$ can well distinguish between landslides exhibiting catastrophic failures from those without catastrophic failures. A higher threshold may reduce the reliability of alerts for failure cases, while a lower threshold could lead to more false alarms. Figure 11b presents the distribution of peak values of dimensionless velocity and acceleration. Similarly, we derive the threshold of $v_n = 2.7$ and $a_n = 1.5$ to differentiate between landslides with catastrophic failures and those without. In summary, for the TA-based method, we set the tangential angle threshold to $\alpha = 70^\circ$, and for the VA-based method, we set this threshold as the combination of $v_n = 2.7$ and $a_n = 1.5$.

We further compare these conventional alert methods with the proposed PH method using data from the Xinmo landslide. Figure 12a illustrates the alert analysis for a specific MP, with the alert-release date defined as the date at which the indicator surpasses its alert threshold. The location of the selected MP is indicated in Figure 3a. This analysis is replicated for 500 randomly selected MPs, yielding corresponding alert release dates as depicted in Figure 12b. The x -axis represents the days before failure when an alert signal is triggered by each method, and

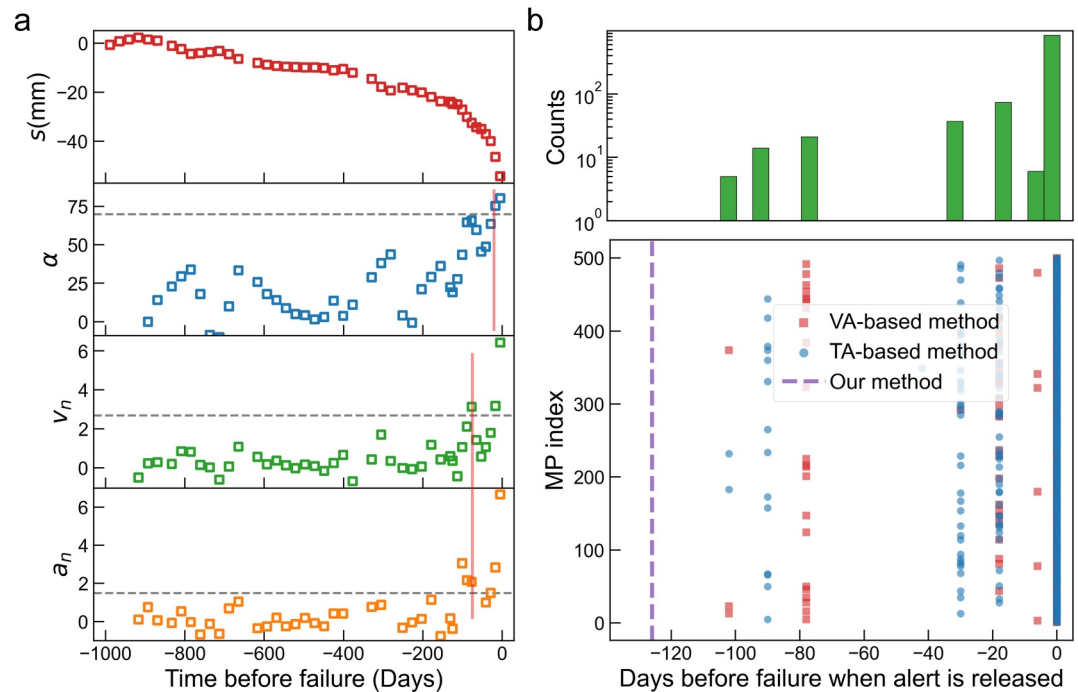


Figure 12. Landslide alert via conventional methods. (a) Evolution of cumulative displacement s , tangential angle α , normalized velocity v_n and acceleration a_n for a selected MP. The location of the selected MP is indicated in Figure 3a. Dotted lines and solid lines respectively indicate the alert thresholds and alert release dates for different methods. (b) Bottom panel: days before failure when an alert is released for 500 randomly selected MPs. Upper panel: histogram of days to failure based on conventional methods. The purple dotted line indicates the alert release date by using our method.

monitoring points that do not provide effective alert signals are assigned a value of 0. It is found that, when assessed through conventional alert methods, most MPs lack the essential information required for effective landslide alerts, and the earliest alert date achieved by these methods still lags behind the prediction from our PH method. To the best of our knowledge, few reliable landslide-alert methods are currently tailored specifically for remote-sensing data. In this context, our proposed method provides an effective early warning approach by analyzing the spatiotemporal evolution of slope deformation. This is particularly advantageous in mountainous regions with steep terrain or areas where in situ monitoring is challenging or unfeasible (Zeng et al., 2024).

4.2. Influence of Spatial and Temporal Resolution

Due to inherent limitations in the InSAR technique and many other remote-sensing methods, these approaches can face challenges with the temporal and spatial resolution of monitoring data (Casagli et al., 2023). In terms of spatial resolution, while the development of remote-sensing techniques enables large-scale continuous monitoring, factors such as the number and quality of the source SAR images as well as environmental conditions such as clouds, snow, crops, and vegetation can significantly impact the spatial resolution of the monitoring data (Casagli et al., 2023; Le Breton et al., 2021). To assess the robustness of our proposed method under these conditions, we assume that some MPs are absent for unknown reasons and employ three different spatial sampling strategies: random spatial sampling, Poisson disk sampling, and area removal. In random spatial sampling, different proportions of MPs are randomly removed, and persistent homology analysis is performed on each realization. As shown in Figure 13, the proposed method can effectively quantify the spatiotemporal evolution of slope deformation with minor deviations even when up to 40% of MPs are randomly removed. Poisson disk sampling removes MPs while ensuring a minimum distance d_{\min} between them, creating a more homogeneous field from the available monitoring data, as seen in the insets of Figure 14. This approach is particularly useful for defining homogeneous kinematic domains in heterogeneously distributed fields. Figure 14 shows that under different choices of d_{\min} , our proposed method can generate reliable early warning signals, indicating that varying spatial resolutions have little influence on the method's effectiveness. Under the condition of Poisson disk sampling, the cutoff distance L_c for defining the MPN is set as $1.5d_{\min}$. It is worth noting that in Figures 13 and 14,

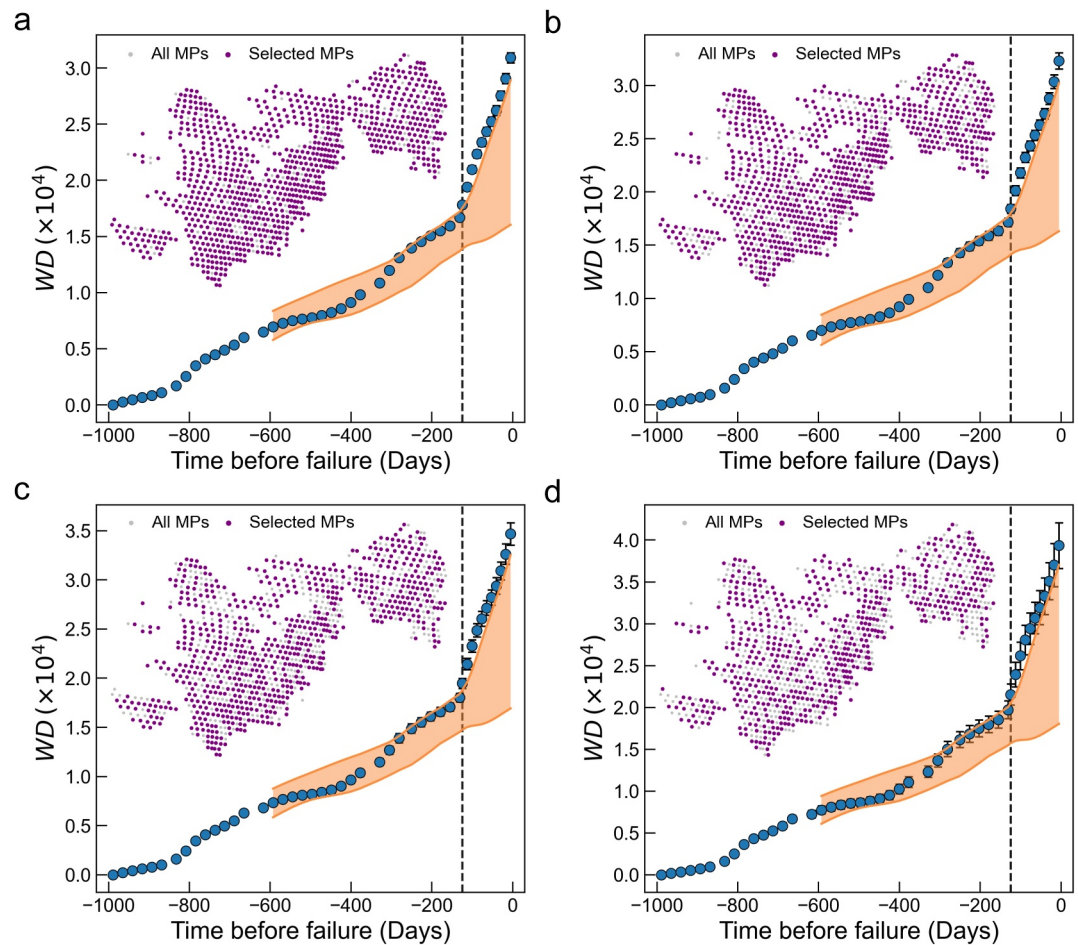


Figure 13. The evolution of WD calculated when the proportion r of MPs are randomly removed: (a) $r = 10\%$, (b) $r = 20\%$, (c) $r = 30\%$, and (d) $r = 40\%$. Error bars indicate standard deviations over 10 individual computations. Gray dotted lines stand for the early warning dates detected by the 3σ criteria. The inserts show the corresponding distributions of selected MPs within one calculation.

we calculate WD and 3σ region and determine the alert date at each realization of the spatial sampling. The shown WD and 3-sigma region are averaged over different realizations, and the alert date (vertical dashed line) remains consistent among different realizations.

Compared to the above two strategies, the area removal strategy directly removes MPs inside a large continuum area. As shown in the insets of Figure 15, we randomly select one MP and define a square area with a dimension of $200\text{ m} \times 200\text{ m}$ around it. All MPs that are located within this area are then removed. Figure 15 shows the results of four independent calculations, which demonstrate that the proposed PH method can still achieve reasonable performance when large areas of MPs are missing. This feature is intriguingly appealing for the application of this method to remote landslide sites located within high mountain canyon regions or highly vegetated environments (R. Guo et al., 2021; Tong & Schmidt, 2016). Such areas usually experience diminished spatial coverage in the InSAR maps due to high decorrelation (low coherence).

Regarding the temporal resolution, due to the limitation of revisit time, InSAR cannot detect large displacements (exceeding half the radar wavelength). This means that if a monitoring point is moving too fast between two subsequent acquisitions, the resulting phase aliasing may underestimate the real displacement, particularly in the vicinity of catastrophic failures (Desai et al., 2023; Handwerger et al., 2022; Manconi, 2021; Warrick et al., 2019). Therefore, while the spatiotemporal evolution rate of landslides near the catastrophic failure may be underestimated, what we have shown in this work is a lower bound, and a stronger early warning signal is expected with higher time resolution data.

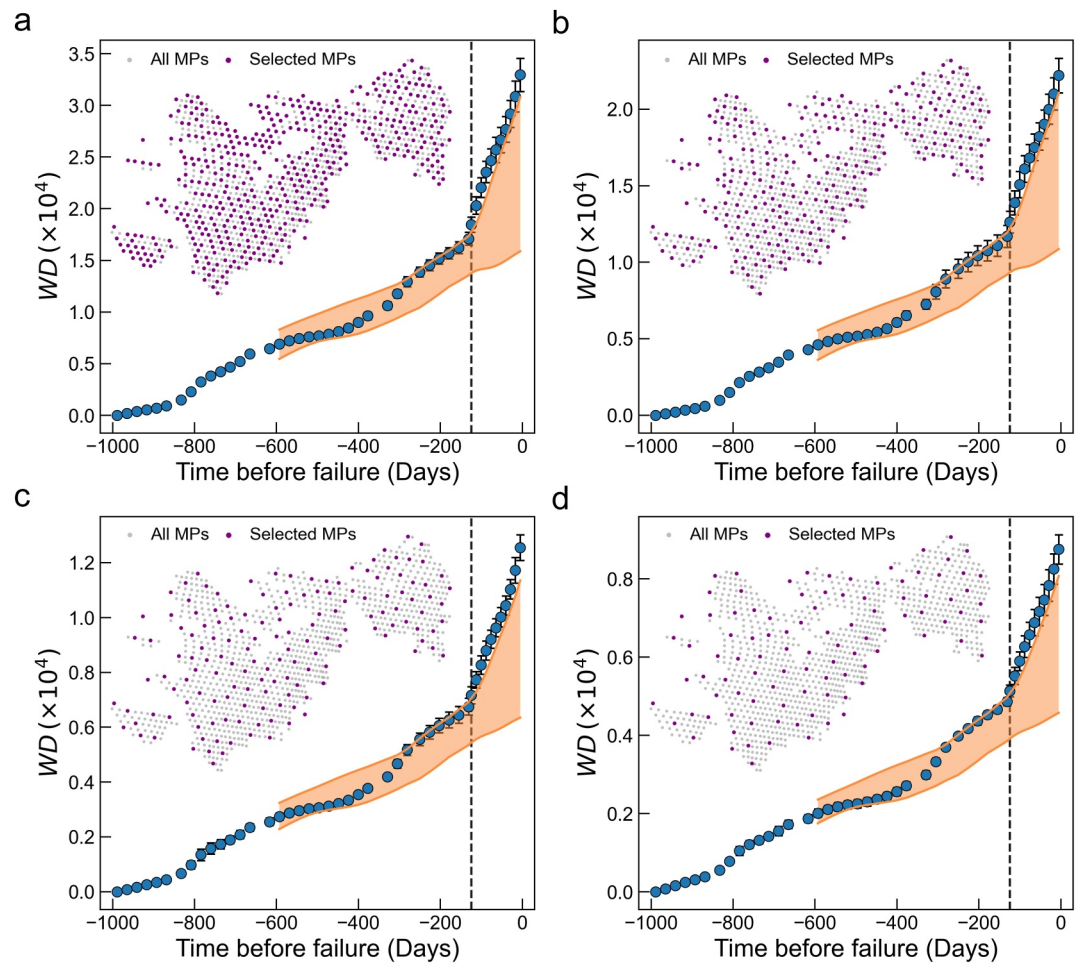


Figure 14. The evolution of WD when MPs are selected using Poisson disk sampling with the minimum distance of (a) $d_{\min} = 15$ m, (b) $d_{\min} = 20$ m, (c) $d_{\min} = 30$ m, and (d) $d_{\min} = 40$ m. Error bars indicate standard deviations over 10 computations, and gray dotted lines stand for the early warning dates detected by the 3σ criteria. The inserts show the corresponding distributions of selected MPs within one calculation.

Moreover, while in this study we are focusing on revealing early warning signals long before the occurrence of catastrophic failure, the proposed PH method offers valuable insights by quantifying the spatiotemporal evolution of slope deformation, which would contribute to the future development of methods capable of predicting precise failure dates. Currently, the most reliable methods for predicting the precise failure dates of landslides rely on the slope displacement and its derivatives (velocity and acceleration) (Intrieri et al., 2019), such as the commonly used inverse-velocity method (Fukuzono, 1985; Intrieri et al., 2018; Leinauer et al., 2023). However, in regions where in situ monitoring is not feasible, the revisit time of many remote sensing techniques, such as InSAR, often limits their ability to capture large displacements and makes it difficult to predict precise failure dates in such areas.

Fortunately, recent years have witnessed a tremendous improvement in reducing the revisit time of satellites, for example, the combination of geosynchronous SAR systems and SAR microsatellites, which holds the potential for reducing the revisit time to hours (Casagli et al., 2023; Xiao et al., 2020). Moreover, integrating satellite InSAR data and satellite optical images can significantly enhance the spatiotemporal resolution of remote-sensing monitoring and provide deeper insight into the complex evolution of landslides (Lacroix et al., 2020; Stumpf et al., 2017; Xiong et al., 2020). In this context, a key focus of future research is to incorporate the proposed PH method and multi-source monitoring data to examine the spatiotemporal evolution of slope deformation, with the hope of uncovering crucial kinematic parameters that can aid in developing accurate methods for predicting the time of failure.

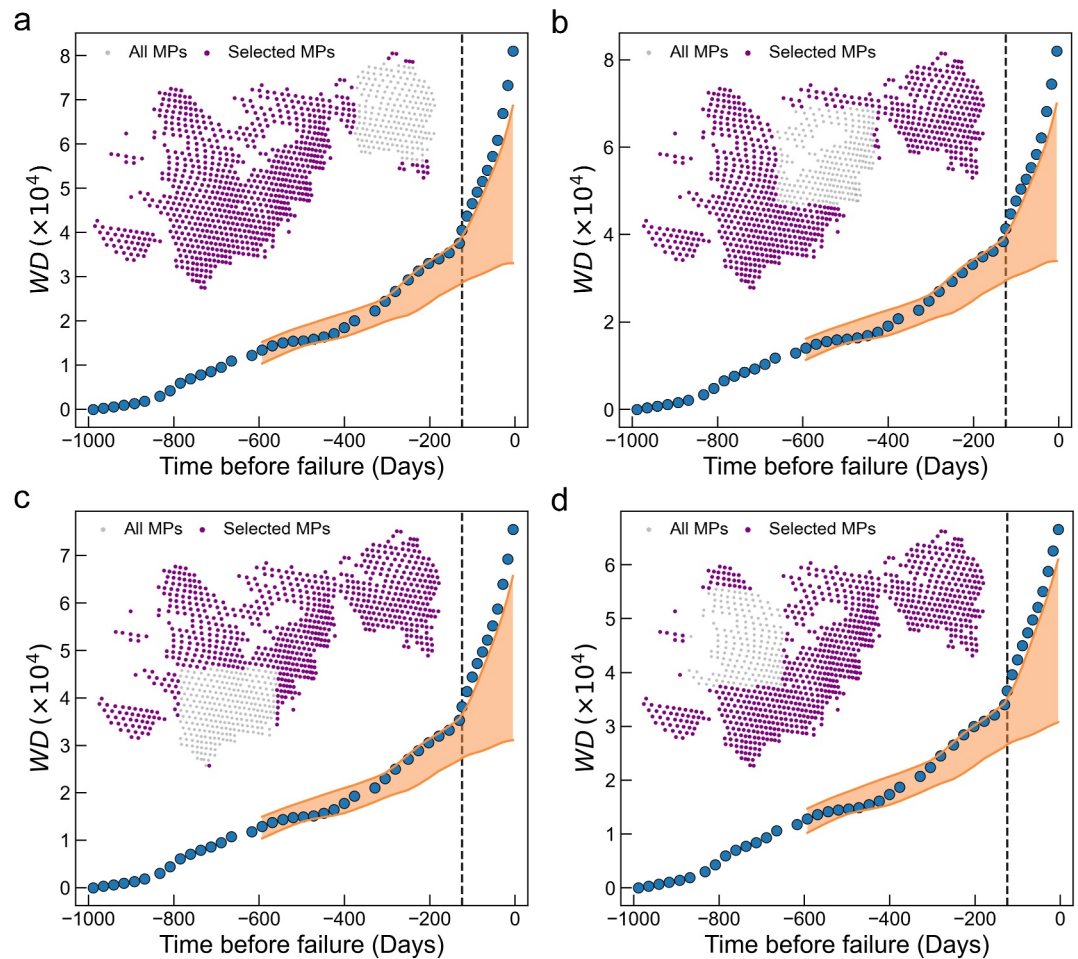


Figure 15. (a–d) The evolution of WD when some MPs inside a large area are removed. The inserts show the corresponding distributions of selected MPs, and gray dotted lines stand for the early warning dates detected by the 3σ criteria. Different subfigures represent different choices of removed areas.

5. Conclusion

In summary, the proposed PH-based method, which integrates monitoring data covering the entire slope, allows for the quantification of the spatiotemporal evolution of ground motion and reveals precursors that indicate potential landslide occurrence. To the best of the authors' knowledge, this is the first instance in which the spatiotemporal evolution of the deformation field at the slope scale has been quantitatively measured. The method generates precursory signals 125 days, 127 days, and 41 days before the Xinmo, Mud Creek, and Longjing landslides, respectively. These early warning signals are much earlier than in many existing studies (Desai et al., 2023; Intrieri et al., 2018; Ju et al., 2020). The findings of this study highlight the essential role of the spatiotemporal evolution of slope deformation in predicting impending landslides. Furthermore, given the consensus that precipitation is a crucial part in inferring landslide occurrence (Cohen-Waeber et al., 2018; Handwerger et al., 2022), incorporating the proposed method with rainfall prediction is vital for improving landslide forecasts.

Considering the complexity of natural landslides, we do not claim that our method is universally applicable to all types of landslides under every circumstance. Instead, we believe that incorporating the proposed method into existing EWS can lay a foundation for future advancements in landslide risk management. More importantly, significant progress in monitoring techniques has led to the generation of vast amounts of data covering various Earth- and space-related aspects, such as climate changes, natural hazards, and solar radiation (Casagli et al., 2023). While these high-resolution monitoring data undoubtedly contain valuable information about

ongoing processes, the rapid increase in data volume and complexity presents considerable challenges for efficiently deciphering underlying causal structures. In this context, our method offers a promising avenue to better investigate the spatiotemporal structures within the ever-growing big data, potentially leading to improved understanding of numerous Earth- and space-related phenomena.

Conflict of Interest

The authors declare no conflicts of interest relevant to this study.

Data Availability Statement

The processed InSAR data reported in this study can be accessed at Mei (2024).

Acknowledgments

We acknowledge the financial support from the National Natural Science Foundation of China (Grants 52322907, 52179141, 12272334, 11972030), the Key Program of Science and Technology of Yunnan Province (Grants 202202AF080004, 202203AA080009), and the Research Grants Council of Hong Kong (GRF I6208720, CRF C7082-22G). The numerical calculations in this work have been performed on the supercomputing system in the Supercomputing Center of Wuhan University. We thank the editor and the anonymous reviewers for their insightful and constructive comments, which have greatly contributed to improving our manuscript.

References

- Aminikhanghahi, S., & Cook, D. J. (2017). A survey of methods for time series change point detection. *Knowledge and Information Systems*, 51(2), 339–367. <https://doi.org/10.1007/s10115-016-0987-z>
- Baule, A., Morone, F., Herrmann, H. J., & Makse, H. A. (2018). Edwards statistical mechanics for jammed granular matter. *Reviews of Modern Physics*, 90(1), 15006. <https://doi.org/10.1103/RevModPhys.90.015006>
- Bell, A. F. (2018). Predictability of landslide timing from quasi-periodic precursory earthquakes. *Geophysical Research Letters*, 45(4), 1860–1869. <https://doi.org/10.1002/2017GL076730>
- Berardino, P., Fornaro, G., Lanari, R., & Sansosti, E. (2002). A new algorithm for surface deformation monitoring based on small baseline differential SAR interferograms. *IEEE Transactions on Geoscience and Remote Sensing*, 40(11), 2375–2383. <https://doi.org/10.1109/TGRS.2002.803792>
- Bhuyan, K., Rana, K., Ferrer, J. V., Cotton, F., Ozturk, U., Catani, F., & Malik, N. (2024). Landslide topology uncovers failure movements. *Nature Communications*, 15(1), 1–13. <https://doi.org/10.1038/s41467-024-46741-7>
- Casagli, N., Intrieri, E., Tofani, V., Gigli, G., & Raspini, F. (2023). Landslide detection, monitoring and prediction with remote-sensing techniques. *Nature Reviews Earth & Environment*, 4(1), 51–64. <https://doi.org/10.1038/s43017-022-00373-x>
- Chen, K. T., & Wu, J. H. (2018). Simulating the failure process of the Xinmo landslide using discontinuous deformation analysis. *Engineering Geology*, 239(November 2017), 269–281. <https://doi.org/10.1016/j.enggeo.2018.04.002>
- Chen, M., & Jiang, Q. (2020). An early warning system integrating time-of-failure analysis and alert procedure for slope failures. *Engineering Geology*, 272(August), 105629. <https://doi.org/10.1016/j.enggeo.2020.105629>
- Chong, S., De-jie, L., Kai-hua, C., & Jia-wen, Z. (2016). Failure mechanism and stability analysis of the Zhenggang landslide in Yunnan Province of China using 3D particle flow code simulation. *Journal of Mountain Science*, 13(5), 891–905. <https://doi.org/10.1007/s11629-014-3399-0>
- Cohen-Waeber, J., Bürgmann, R., Chaussard, E., Giannico, C., & Ferretti, A. (2018). Spatiotemporal patterns of precipitation-modulated landslide deformation from independent component analysis of InSAR time series. *Geophysical Research Letters*, 45(4), 1878–1887. <https://doi.org/10.1002/2017GL075950>
- Crosta, G. B., & Agliardi, F. (2002). How to obtain alert velocity thresholds for large rockslides. *Physics and Chemistry of the Earth*, 27(36), 1557–1565. [https://doi.org/10.1016/S1474-7065\(02\)00177-8](https://doi.org/10.1016/S1474-7065(02)00177-8)
- Cui, M., Wang, J., & Yue, M. (2019). Machine learning-based anomaly detection for load forecasting under cyberattacks. *IEEE Transactions on Smart Grid*, 10(5), 5724–5734. <https://doi.org/10.1109/tsg.2018.2890809>
- Desai, V. D., Fazelpour, F., Handwerker, A. L., & Daniels, K. E. (2023). Forecasting landslides using community detection on geophysical satellite data. *Physical Review E*, 108(1), 014901. <https://doi.org/10.1103/PhysRevE.108.014901>
- Deshpande, N. S., Furbish, D. J., Arratia, P. E., & Jerolmack, D. J. (2021). The perpetual fragility of creeping hillslopes. *Nature Communications*, 12(1), 1–7. <https://doi.org/10.1038/s41467-021-23979-z>
- Ding, Q., Guo, C., Fan, X., Liu, X., Gong, X., Zhou, W., & Ma, G. (2023). Multi-source monitoring data helps revealing and quantifying the excavation-induced deterioration of rock mass. *Engineering Geology*, 325(May), 107281. <https://doi.org/10.1016/j.enggeo.2023.107281>
- Di Traglia, F., De Luca, C., Manzo, M., Nolesini, T., Casagli, N., Lanari, R., & Casu, F. (2021). Joint exploitation of space-borne and ground-based multitemporal InSAR measurements for volcano monitoring: The Stromboli volcano case study. *Remote Sensing of Environment*, 260(March), 112441. <https://doi.org/10.1016/j.rse.2021.112441>
- Fan, X., Xu, Q., Liu, J., Subramanian, S. S., He, C., Zhu, X., & Zhou, L. (2019). Successful early warning and emergency response of a disastrous rockslide in Guizhou province, China. *Landslides*, 16(12), 2445–2457. <https://doi.org/10.1007/s10346-019-01269-6>
- Fan, X., Xu, Q., Scaringi, G., Dai, L., Li, W., Dong, X., et al. (2017). Failure mechanism and kinematics of the deadly June 24th 2017 Xinmo landslide, Maoxian, Sichuan, China. *Landslides*, 14(6), 2129–2146. <https://doi.org/10.1007/s10346-017-0907-7>
- Ferrari, A., Richard, C., Bourrier, A., & Bouchikhi, I. (2023). Online change-point detection with kernels. *Pattern Recognition*, 133, 109022. <https://doi.org/10.1016/j.patcog.2022.109022>
- Finnegan, N. J., Brodsky, E. E., Savage, H. M., Nereson, A. L., & Murphy, C. R. (2022). Seasonal slow landslide displacement is accommodated by mm-scale stick-slip events. *Geophysical Research Letters*, 49(20). <https://doi.org/10.1029/2022GL099548>
- Fukuzono, T. (1985). A method to predict the time of slope failure caused by rainfall using the inverse number of velocity of surface displacement. *Landslides*, 22(2), 8–13_1. https://doi.org/10.3313/jls1964.22.2_8
- Gariano, S. L., & Guzzetti, F. (2016). Landslides in a changing climate. *Earth-Science Reviews*, 162, 227–252. <https://doi.org/10.1016/j.earscirev.2016.08.011>
- Ghosh, A., Budrikis, Z., Chikkadi, V., Sellerio, A. L., Zapperi, S., & Schall, P. (2017). Direct observation of percolation in the yielding transition of colloidal glasses. *Physical Review Letters*, 118(14), 148001. <https://doi.org/10.1103/PhysRevLett.118.148001>
- Giri, P., Ng, K., & Phillips, W. (2019). Wireless sensor network system for landslide monitoring and warning. *IEEE Transactions on Instrumentation and Measurement*, 68(4), 1210–1220. <https://doi.org/10.1109/TIM.2018.2861999>
- Goswami, B., Boers, N., Rheinwalt, A., Marwan, N., Heitzig, J., Breitenbach, S. F. M., & Kurths, J. (2018). Abrupt transitions in time series with uncertainties. *Nature Communications*, 9(1), 1–10. <https://doi.org/10.1038/s41467-017-02456-6>

- Guo, C., Ma, G., Xiao, H., Zhou, W., Chen, H., Zhou, Z., & Cheng, X. (2022). Displacement back analysis of reservoir landslide based on multi-source monitoring data: A case study of the cheyiping landslide in the Lancang River basin, China. *Remote Sensing*, *14*(11), 2683. <https://doi.org/10.3390/rs14112683>
- Guo, R., Li, S., Chen, Y., Li, X., & Yuan, L. (2021). Identification and monitoring landslides in Longitudinal Range-Gorge Region with InSAR fusion integrated visibility analysis. *Landslides*, *18*(2), 551–568. <https://doi.org/10.1007/s10346-020-01475-7>
- Handwerger, A. L., Fielding, E. J., Sangha, S. S., & Bekaert, D. P. S. (2022). Landslide sensitivity and response to precipitation changes in wet and dry climates. *Geophysical Research Letters*, *49*(13), 1–12. <https://doi.org/10.1029/2022GL099499>
- Handwerger, A. L., Huang, M. H., Fielding, E. J., Booth, A. M., & Bürgmann, R. (2019). A shift from drought to extreme rainfall drives a stable landslide to catastrophic failure. *Scientific Reports*, *9*(1), 1–12. <https://doi.org/10.1038/s41598-018-38300-0>
- Hiraoka, Y., Nakamura, T., Hirata, A., Escolar, E. G., Matsue, K., & Nishiura, Y. (2016). Hierarchical structures of amorphous solids characterized by persistent homology. *Proceedings of the National Academy of Sciences of the United States of America*, *113*(26), 7035–7040. <https://doi.org/10.1073/pnas.1520877113>
- Hu, W., Scaringi, G., Xu, Q., & Huang, R. (2018). Acoustic emissions and microseismicity in granular slopes prior to failure and flow-like motion: The potential for early warning. *Geophysical Research Letters*, *45*(19), 10406–10415. <https://doi.org/10.1029/2018GL079724>
- Huang, R. (2009). Some catastrophic landslides since the twentieth century in the southwest of China. *Landslides*, *6*(1), 69–81. <https://doi.org/10.1007/s10346-009-0142-y>
- Hungr, O., Leroueil, S., & Picarelli, L. (2014). The Varnes classification of landslide types, an update. *Landslides*, *11*(2), 167–194. <https://doi.org/10.1007/s10346-013-0436-y>
- Intrieri, E., Carlà, T., & Gigli, G. (2019). Forecasting the time of failure of landslides at slope-scale: A literature review. *Earth-Science Reviews*, *193*(September 2018), 333–349. <https://doi.org/10.1016/j.earscirev.2019.03.019>
- Intrieri, E., Raspini, F., Fumagalli, A., Lu, P., Del Conte, S., Farina, P., et al. (2018). The Maoxian landslide as seen from space: Detecting precursors of failure with Sentinel-1 data. *Landslides*, *15*(1), 123–133. <https://doi.org/10.1007/s10346-017-0915-7>
- Iverson, R. M. (2000). Landslide triggering by rain infiltration. *Water Resources Research*, *36*(7), 1897–1910. <https://doi.org/10.1029/2000WR900090>
- Jaboyedoff, M., Oppikofer, T., Abellán, A., Derron, M. H., Loye, A., Metzger, R., & Pedrazzini, A. (2012). Use of LIDAR in landslide investigations: A review. *Natural Hazards*, *61*(1), 5–28. <https://doi.org/10.1007/s11069-010-9634-2>
- Ju, N., Huang, J., He, C., Van Asch, T. W. J., Huang, R., Fan, X., et al. (2020). Landslide early warning, case studies from Southwest China. *Engineering Geology*, *279*(July), 105917. <https://doi.org/10.1016/j.enggeo.2020.105917>
- Kirschbaum, D., Kapnick, S. B., Stanley, T., & Pascale, S. (2020). Changes in extreme precipitation and landslides over high mountain Asia. *Geophysical Research Letters*, *47*(4), 1–9. <https://doi.org/10.1029/2019GL085347>
- Kothari, U. C., & Momayez, M. (2018). New approaches to monitoring, analyzing and predicting slope instabilities. *Journal of Geology and Mining Research*, *10*(1), 1–14. <https://doi.org/10.5897/jgmr2017.0272>
- Kou, B., Cao, Y., Li, J., Xia, C., Li, Z., Dong, H., et al. (2018). Translational and rotational dynamical heterogeneities in granular systems. *Physical Review Letters*, *121*(1), 18002. <https://doi.org/10.1103/PhysRevLett.121.018002>
- Kovacev-Nikolic, V., Bubenik, P., Nikolic, D., & Heo, G. (2016). Using persistent homology and dynamical distances to analyze protein binding. *Statistical Applications in Genetics and Molecular Biology*, *15*(1), 19–38. <https://doi.org/10.1515/sagmb-2015-0057>
- Lacroix, P., Handwerger, A. L., & Bièvre, G. (2020). Life and death of slow-moving landslides. *Nature Reviews Earth & Environment*, *1*(8), 404–419. <https://doi.org/10.1038/s43017-020-0072-8>
- Le Breton, M., Bontemps, N., Guillemot, A., Baillet, L., & Larose, É. (2021). Landslide monitoring using seismic ambient noise correlation: Challenges and applications. *Earth-Science Reviews*, *216*(January), 103518. <https://doi.org/10.1016/j.earscirev.2021.103518>
- Lei, Q., & Sornette, D. (2023). A stochastic dynamical model of slope creep and failure. *Geophysical Research Letters*, *50*(11), 1–11. <https://doi.org/10.1029/2022GL102587>
- Lei, Q., Sornette, D., Yang, H., & Loew, S. (2023). Real-time forecast of catastrophic landslides via Dragon-King detection. *Geophysical Research Letters*, *50*(6), 1–10. <https://doi.org/10.1029/2022GL100832>
- Leinauer, J., Weber, S., Ciccoira, A., Beutel, J., & Krautblatter, M. (2023). An approach for prospective forecasting of rock slope failure time. *Communications Earth & Environment*, *4*(1), 253. <https://doi.org/10.1038/s43247-023-00909-z>
- Li, M., Liu, R. R., Lü, L., Hu, M. B., Xu, S., & Zhang, Y. C. (2021). Percolation on complex networks: Theory and application. *Physics Reports*, *907*, 1–68. <https://doi.org/10.1016/j.physrep.2020.12.003>
- Li, S., Xu, W., & Li, Z. (2022). Review of the SBAS InSAR Time-series algorithms, applications, and challenges. *Geodesy and Geodynamics*, *13*(2), 114–126. <https://doi.org/10.1016/j.geog.2021.09.007>
- Liu, J., Hao, R., Liu, Q., & Guo, W. (2023). Prediction of remaining useful life of rolling element bearings based on LSTM and exponential model. *International Journal of Machine Learning and Cybernetics*, *14*(4), 1567–1578. <https://doi.org/10.1007/s13042-023-01807-8>
- Manconi, A. (2021). How phase aliasing limits systematic space-borne DInSAR monitoring and failure forecast of alpine landslides. *Engineering Geology*, *287*, 106094. <https://doi.org/10.1016/j.enggeo.2021.106094>
- Mei, J. (2024). Data for: Persistent homology for landslide precursors [Dataset]. *Zenodo*. <https://doi.org/10.5281/zenodo.14029479>
- Mei, J., Ma, G., Cao, W., Wu, T., & Zhou, W. (2025). Graph neural network unveils the spatiotemporal evolution of structural defects in sheared granular materials. *International Journal of Plasticity*, *184*(September 2024), 104218. <https://doi.org/10.1016/j.ijplas.2024.104218>
- Mei, J., Ma, G., Liu, J., Nicot, F., & Zhou, W. (2023). Modeling shear-induced solid-liquid transition of granular materials using persistent homology. *Journal of the Mechanics and Physics of Solids*, *176*(December 2022), 105307. <https://doi.org/10.1016/j.jmps.2023.105307>
- Moretto, S., Bozzano, F., & Mazzanti, P. (2021). The role of satellite insar for landslide forecasting: Limitations and openings. *Remote Sensing*, *13*(18), 1–31. <https://doi.org/10.3390/rs13183735>
- Murphy, C. R., Finnegan, N. J., & Oberle, F. K. J. (2022). Vadose zone thickness limits pore-fluid pressure rise in a large, slow-moving earthflow. *Journal of Geophysical Research: Earth Surface*, *127*(6), 1–20. <https://doi.org/10.1029/2021JF006415>
- Noda, H., & Chang, C. (2023). Tertiary creep behavior for various rate- and state-dependent friction laws. *Earth and Planetary Science Letters*, *619*, 118314. <https://doi.org/10.1016/j.epsl.2023.118314>
- Notti, D., Wrzesniak, A., Dematteis, N., Lollino, P., Fazio, N. L., Zucca, F., & Giordan, D. (2021). A multidisciplinary investigation of deep-seated landslide reactivation triggered by an extreme rainfall event: A case study of the Monesi di Mendatica landslide, Ligurian Alps. *Landslides*, *18*(7), 2341–2365. <https://doi.org/10.1007/s10346-021-01651-3>
- Oya, S., Imaizumi, F., & Takayama, S. (2024). Field monitoring of pore water pressure in fully and partly saturated debris flows at Ohya landslide scar, Japan. *Earth Surface Dynamics*, *12*(1), 67–86. <https://doi.org/10.5194/esurf-12-67-2024>
- Papadopoulos, L., Porter, M. A., Daniels, K. E., & Bassett, D. S. (2018). Network analysis of particles and grains. *Journal of Complex Networks*, *6*(4), 485–565. <https://doi.org/10.1093/COMNET/CNY005>

- Paul, K., Bhattacharya, P., & Misra, S. (2024). Frictional control on accelerating creep during the slow-to-fast transition of rainfall-induced catastrophic landslides. *Journal of Geophysical Research: Earth Surface*, 129(1). <https://doi.org/10.1029/2023JF007213>
- Picarelli, L., Lacasse, S., & Ho, K. K. S. (2021). The impact of climate change on landslide hazard and risk. In K. Sassa, M. Mikoš, S. Sassa, P. T. Bobrowsky, K. Takara, & K. Dang (Eds.), *Understanding and reducing landslide disaster risk: Volume 1 Sendai landslide partnerships and Kyoto landslide commitment* (pp. 131–141). Springer International Publishing. https://doi.org/10.1007/978-3-030-60196-6_6
- Piciullo, L., Calvello, M., & Cepeda, J. M. (2018). Territorial early warning systems for rainfall-induced landslides. *Earth-Science Reviews*, 179(February), 228–247. <https://doi.org/10.1016/j.earscirev.2018.02.013>
- Poli, P. (2017). Creep and slip: Seismic precursors to the Nuugaatsiaq landslide (Greenland). *Geophysical Research Letters*, 44(17), 8832–8836. <https://doi.org/10.1002/2017GL075039>
- Rana, K., Ozturk, U., & Malik, N. (2021). Landslide geometry reveals its trigger. *Geophysical Research Letters*, 48(4), 1–8. <https://doi.org/10.1029/2020GL090848>
- Rouet-Leduc, B., Jolivet, R., Dalaison, M., Johnson, P. A., & Hulbert, C. (2021). Autonomous extraction of millimeter-scale deformation in InSAR time series using deep learning. *Nature Communications*, 12(1), 1–11. <https://doi.org/10.1038/s41467-021-26254-3>
- Ruggieri, E., & Antonellis, M. (2016). An exact approach to Bayesian sequential change point detection. *Computational Statistics & Data Analysis*, 97, 71–86. <https://doi.org/10.1016/j.csda.2015.11.010>
- Schönfeldt, E., Winocur, D., Pánek, T., & Korup, O. (2022). Deep learning reveals one of Earth's largest landslide terrain in Patagonia. *Earth and Planetary Science Letters*, 593, 117642. <https://doi.org/10.1016/j.epsl.2022.117642>
- Singh, K., & Tordesillas, A. (2020). Spatiotemporal evolution of a landslide: A transition to explosive percolation. *Entropy*, 22(1), 67. <https://doi.org/10.3390/e22010067>
- Sreejith, K. M., Jasir, M. C. M., Sunil, P. S., Rose, M. S., Saji, A. P., Agrawal, R., et al. (2024). Geodetic evidence for cascading landslide motion triggered by extreme rain events at Joshimath, NW Himalaya. *Geophysical Research Letters*, 51(9). <https://doi.org/10.1029/2023GL106427>
- Stumpf, A., Malet, J. P., & Delacourt, C. (2017). Correlation of satellite image time-series for the detection and monitoring of slow-moving landslides. *Remote Sensing of Environment*, 189, 40–55. <https://doi.org/10.1016/j.rse.2016.11.007>
- Teshebaeva, K., Ehtler, H., Bookhagen, B., & Strecker, M. (2019). Deep-seated gravitational slope deformation (DSGSD) and slow-moving landslides in the southern tien Shan mountains: New insights from InSAR, tectonic and geomorphic analysis. *Earth Surface Processes and Landforms*, 44(12), 2333–2348. <https://doi.org/10.1002/esp.4648>
- Tong, X., & Schmidt, D. (2016). Active movement of the Cascade landslide complex in Washington from a coherence-based InSAR time series method. *Remote Sensing of Environment*, 186, 405–415. <https://doi.org/10.1016/j.rse.2016.09.008>
- Urgilez Vinueza, A., Handwerker, A. L., Bakker, M., & Bogaard, T. (2022). A new method to detect changes in displacement rates of slow-moving landslides using InSAR time series. *Landslides*, 19(9), 2233–2247. <https://doi.org/10.1007/s10346-022-01913-8>
- Warrick, J. A., Ritchie, A. C., Schmidt, K. M., Reid, M. E., & Logan, J. (2019). Characterizing the catastrophic 2017 Mud Creek landslide, California, using repeat structure-from-motion (SfM) photogrammetry. *Landslides*, 16(November 2018), 1201–1219. <https://doi.org/10.1007/s10346-019-01160-4>
- Wasserman, L. (2018). Topological data analysis. *Annual Review of Statistics and Its Application*, 5(1), 501–532. <https://doi.org/10.1146/annurev-statistics-031017-100045>
- Xiao, P., Liu, B., & Guo, W. (2020). ConGaLSAR: A constellation of geostationary and low Earth orbit synthetic aperture radar. *IEEE Geoscience and Remote Sensing Letters*, 17(12), 2085–2089. <https://doi.org/10.1109/LGRS.2019.2962574>
- Xiong, Z., Feng, G., Feng, Z., Miao, L., Wang, Y., Yang, D., & Luo, S. (2020). Pre- and post-failure spatial-temporal deformation pattern of the Baige landslide retrieved from multiple radar and optical satellite images. *Engineering Geology*, 279(February), 105880. <https://doi.org/10.1016/j.enggeo.2020.105880>
- Xu, Q., Yuan, Y., Zeng, Y., & Hack, R. (2011). Some new pre-warning criteria for creep slope failure. *Science China Technological Sciences*, 54(1 SUPPL), 210–220. <https://doi.org/10.1007/s11431-011-4640-5>
- Ye, X., Zhu, H., Chang, F., Xie, T., Tian, F., Zhang, W., & Catani, F. (2024). Revisiting spatiotemporal evolution process and mechanism of a giant reservoir landslide during weather extremes. *Engineering Geology*, 332(September 2023), 107480. <https://doi.org/10.1016/j.enggeo.2024.107480>
- Yin, Y., Wang, F., & Sun, P. (2009). Landslide hazards triggered by the 2008 Wenchuan earthquake, Sichuan, China. *Landslides*, 6(2), 139–152. <https://doi.org/10.1007/s10346-009-0148-5>
- Youssef, A. M., & Pourghasemi, H. R. (2021). Landslide susceptibility mapping using machine learning algorithms and comparison of their performance at Abha Basin, Asir Region, Saudi Arabia. *Geoscience Frontiers*, 12(2), 639–655. <https://doi.org/10.1016/j.gsf.2020.05.010>
- Yu, C., Li, Z., Penna, N. T., & Crippa, P. (2018). Generic atmospheric correction model for interferometric synthetic aperture radar observations. *Journal of Geophysical Research: Solid Earth*, 123(10), 9202–9222. <https://doi.org/10.1029/2017JB015305>
- Zeng, P., Feng, B., Dai, K., Li, T., Fan, X., & Sun, X. (2024). Can satellite InSAR innovate the way of large landslide early warning? *Engineering Geology*, 342(February), 107771. <https://doi.org/10.1016/j.enggeo.2024.107771>
- Zhang, M., & Shi, W. (2020). A feature difference convolutional neural network-based change detection method. *IEEE Transactions on Geoscience and Remote Sensing*, 58(10), 7232–7246. <https://doi.org/10.1109/TGRS.2020.2981051>
- Zhao, B., Su, L., Xu, Q., Li, W., Xu, C., & Wang, Y. (2023). A review of recent earthquake-induced landslides on the Tibetan Plateau. *Earth-Science Reviews*, 244(February), 104534. <https://doi.org/10.1016/j.earscirev.2023.104534>
- Zhou, Q., Tang, H., Turowski, J. M., Braun, J., Dietze, M., Walter, F., et al. (2024). Benford's law as debris flow detector in seismic signals. *Journal of Geophysical Research: Earth Surface*, 129(9), 1–17. <https://doi.org/10.1029/2024JF007691>
- Zhou, S., Tordesillas, A., Intrieri, E., Di Traglia, F., Qian, G., & Catani, F. (2022). Pinpointing early signs of impending slope failures from space. *Journal of Geophysical Research: Solid Earth*, 127(2). <https://doi.org/10.1029/2021JB022957>
- Zhu, X. (2013). Persistent homology: An introduction and a new text representation for natural language processing. *IJCAI International Joint Conference on Artificial Intelligence*, 1953–1959.